HEALTH AND MEDICINE

Phagocytosis of Wnt inhibitor SFRP4 by late wound macrophages drives chronic Wnt activity for fibrotic skin healing

Denise Gay[1,2,*†], Giulia Ghinatti[1,2,3,4], Christian F. Guerrero-Juarez[5], Rubén A. Ferrer[6], Federica Ferri[1,2,3,4], Chae Ho Lim[7], Shohei Murakami[1,2,3,4], Nathalie Gault[1,2,3,4], Vilma Barroca[1,2,3,4], Isabelle Rombeau[8], Philippe Mauffrey[1,2,3], Lamya Irbah[1,2,3], Elsa Treffeisen[9], Sandra Franz[6,10], Alexandre Boissonnas[11], Christophe Combadière[11], Mayumi Ito[7], Maksim V. Plikus[5], Paul-Henri Romeo[1,2,3,4†]

Human and murine skin wounding commonly results in fibrotic scarring, but the murine wounding model wound-induced hair neogenesis (WIHN) can frequently result in a regenerative repair response. Here, we show in single-cell RNA sequencing comparisons of semi-regenerative and fibrotic WIHN wounds, increased expression of phagocytic/lysosomal genes in macrophages associated with predominance of fibrotic myofibroblasts in fibrotic wounds. Investigation revealed that macrophages in the late wound drive fibrosis by phagocytizing dermal Wnt inhibitor SFRP4 to establish persistent Wnt activity. In accordance, phagocytosis abrogation resulted in transient Wnt activity and a more regenerative healing. Phagocytosis of SFRP4 was integrin-mediated and dependent on the interaction of SFRP4 with the EDA splice variant of fibronectin. In the human skin condition hidradenitis suppurativa, phagocytosis of SFRP4 by macrophages correlated with fibrotic wound repair. These results reveal that macrophages can modulate a key signaling pathway via phagocytosis to alter the skin wound healing fate.

INTRODUCTION

In many tissues, including lung, liver, kidney, muscle, and skin, injury promotes timed events that result in regeneration or fibrosis (*1*–*5*). Myofibroblasts are commonly invoked in response to damage, and they promote wound contraction, as well as closure, and produce extracellular matrix (ECM) components (*6*). Although considered as the key players in fibrosis, myofibroblasts also have important roles in regenerative repair: as a source of adipocyte progenitors in skin (*7*), patching of muscle (*4*), reconstruction of connective tissue including skin dermis (*8*, *9*), and stem cell support in intestine and stomach (*10*, *11*). Thus, the degree of myofibroblast induction and/or activation might determine the ultimate healing fate as regenerative or fibrotic.

At the molecular level, myofibroblast activity is regulated by multiple signaling pathways, of which the transforming growth factor β (TGFβ) pathway is the most studied. Target genes in this pathway include key ECM and contractile components such as collagens, elastin, fibronectin (FN), and α–smooth muscle actin (αSMA) (*6*, *12*). Thus, controlled activity of TGFβ is essential for ECM restructuring in regeneration; however, chronic escalated induction is considered a key component of fibrogenesis (*13*). The canonical Wnt pathway is also a keystone pathway for myofibroblast fibrogenic activity in numerous tissues (*4*, *14*–*20*). High chronic Wnt activity in overexpression models leads to myofibroblast proliferation and de novo transcription of profibrotic ECM and matrix metalloproteinase genes (*14*–*19*) and, importantly, β-catenin (β-Cat) stabilization of lower-dermis myofibroblasts in young mice has been shown to prevent their transdifferentiation into adipocytes and to promote a fibrogenic environment in skin (*20*). Paradoxically, transient Wnt activity in myofibroblasts has been demonstrated as a criterion for hair neogenesis in skin wound healing (*21*).

Macrophages contribute to all phases of tissue repair, providing essential inflammatory and debris clearance functions during early wounding, which then give way, during the regenerative phase, to functions supporting healing. These include roles not only in stem cell maintenance and differentiation in muscle and liver and angiogenesis and dermal reconstruction in skin but also fibrogenic programs in many tissues (*22*–*26*). Although two major populations, termed pro-inflammatory M1 and proregenerative M2, have been credited with these disparate roles, it has become increasingly apparent that macrophages exhibit remarkable plasticity with regard to their microenvironment, thus complicating this simple categorization (*27*).

During late healing, macrophages secrete essential factors such as platelet-derived growth factor α (PDGFα), interleukin-10 (IL-10), TGFβ, FN, resistin-like molecule α (RELM-α), and vascular endothelial growth factor that drive tissue regeneration and/or fibrosis. Unexpectedly, another established macrophage function, phagocytosis, has received less attention as a potential driver of regeneration/fibrosis, although it is recognized for impeding tumorigenesis and recurring tissue damage via ingestion of tumor and apoptotic cells and pathogens (*28*, *29*), as well as remodeling of local microbiota and ECM components (*30*, *31*).

[1]CEA/DRF/IBFJ/iRCM/LRTS, 92265 Fontenay-aux-Roses cedex, France. [2]Inserm U1074, 92265 Fontenay-aux-Roses cedex, France. [3]Université Paris-Diderot, Paris 7, France. [4]Université Paris-Sud, Paris 11, France. [5]Department of Developmental and Cell Biology, Sue and Bill Gross Stem Cell Research Center, NSF-Simons Center for Multiscale Cell Fate Research, Center for Complex Biological Systems, University of California, Irvine, Irvine, CA 92697, USA. [6]Department of Dermatology, University Leipzig Medical Center, Leipzig, Germany. [7]Ronald O. Perelman Department of Dermatology and Cell Biology, School of Medicine, New York University, New York, NY 10016, USA. [8]Charles River Laboratories, 169 Bois des Oncins, 69210 Saint-Germain-Nuelles, France. [9]Department of Pediatrics, Cohen Children's Medical Center Northwell Health, New Hyde Park, NY 11040, USA. [10]DFG-German Research Council Transregio 67, Leipzig-Dresden, Germany. [11]Sorbonne Université, Inserm, CNRS, Centre d'Immunologie et des Maladies Infectieuses, Cimi-Paris, F-75013, Paris, France.
*Present address: Ronald O. Perelman Department of Dermatology and Cell Biology, School of Medicine, New York University, New York, NY 10016, USA.
†Corresponding author. Email: denise.gay@nyulangone.org (D.G.); paul-henri.romeo@cea.fr (P.-H.R.)

Skin wounding provides an ideal model to address roles for the innate immune system in regenerative versus fibrotic healing. Although wounding typically results in contraction, over-deposition of ECM components, and no adnexal structure regeneration, all hallmarks of fibrosis (*5*), a more regenerative response, with adnexal structure neogenesis, has been documented over the past century (*32*). This phenomenon can be recapitulated in the wound-induced hair neogenesis (WIHN) model, in which transient Wnt activation in myofibroblasts during late healing promotes hair neogenesis (*21*, *33*–*35*). Because the WIHN model can also result in fibrotic scarring, we compared these healing outcomes to interrogate potential roles for macrophages in healing fate determination.

RESULTS

Chronic Wnt activity is associated with fibrotic repair in WIHN$^-$ wounds

In the WIHN wounding model, large full thickness excisions (1 cm^2) can permit the regeneration of de novo hair follicles (termed WIHN$^+$), suggesting a more regenerative environment (Fig. 1A) (*33*). However, large wounds can also result in hairless scars (termed WIHN$^-$). Comparison of WIHN$^-$ and WIHN$^+$ phenotypes during the remodeling phase confirmed that WIHN$^-$ wounds exhibited all the hallmarks of fibrotic repair including significant wound contraction (Fig. 1, A and B), increased collagen deposition (Fig. 1C), and increased transcription of profibrotic genes *Tgfb1*, *Col1a1*, and *FN1* by wound day (WD) 22 (Fig. 1D).

Chronic canonical Wnt activity is a newly established hallmark of fibrotic repair, but transient dermal and then epidermal Wnt activities are known requisites for hair neogenesis (*21*, *33*). To ask whether Wnt longevity correlated with wound phenotype, we compared WIHN$^+$ and WIHN$^-$ wounds for transcription of known dermal Wnt ligand *Wnt2* and Wnt target *Axin2* at WD16, a time point immediately after WIHN$^+$ Wnt activity down-modulation, and at WD22. Wnt activity was elevated in WIHN$^-$ wounds at both time points (Fig. 1D). Examination of dermal nuclear β-Cat localization, a hallmark of Wnt activity, at WD22, confirmed that WIHN$^-$ wounds alone maintained substantial dermal Wnt activity at this late time point (Fig. 1E and fig. S1).

Between WD14 and WD16, all wounds lost their residual scab, signifying completion of reepithelialization (*33*), WIHN$^+$ wounds down-modulated Wnt activity and ECM deposition and began hair neogenesis, while WIHN$^-$ wounds continued high ECM production and Wnt activity through WD22 at least (Fig. 1F). We focused around this transition period, the earliest point during which WIHN phenotype could be assessed, to ask about factors that might affect healing fate.

Single-cell RNA-seq of WD18 WIHN$^+$ and WIHN$^-$ wound dermis shows overrepresentation of fibrotic myofibroblasts in the WIHN$^-$ wound and reveals a phagocytic signature in macrophages

To determine the transcriptome landscape in newly fibrotic and "regenerative" wounds (i.e., exhibiting hair neogenesis, reduced contraction, reduced Wnt, TGFβ signaling activity, and reduced collagen production), we undertook single-cell RNA sequencing (RNA-seq) analysis of whole wound dermis several days after the transition period (WD18). Comparisons revealed significant differences in cellular composition. The WIHN$^+$ RNA-seq analysis (approximately 10,587 cells) comprised multiple highly populated myofibroblast clusters, a

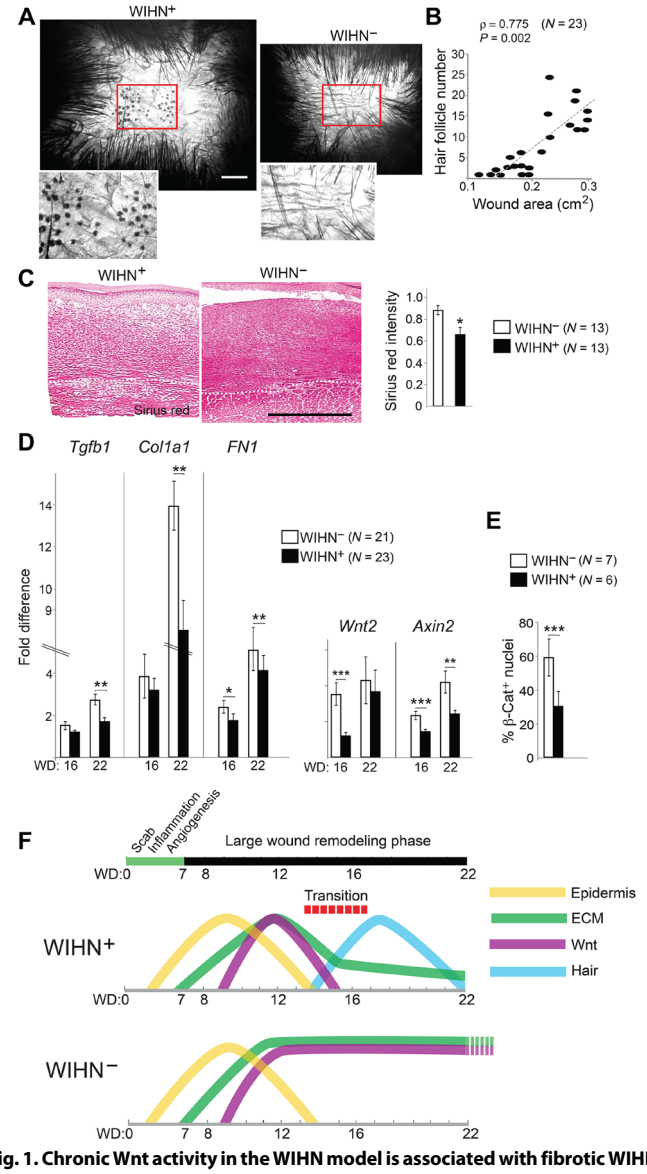

Fig. 1. Chronic Wnt activity in the WIHN model is associated with fibrotic WIHN$^-$ scarring. (**A**) Whole mounts of wild-type (WT; C57BL/6J) WIHN$^+$ (left) and WIHN$^-$ (right) wounds at WD22. Red rectangles define enlarged panels. Scale bar, 1 mm. Representative results from 25 experiments. (**B**) Pearson's correlation between wound area (*x* axis) and numbers of new hair follicles (*y* axis) in WT wounds. Pearson correlation coefficient (ρ) = 0.775, P = 0.002. (**C**) Left: Sirius red staining of WD18 WIHN$^+$ (left) and WIHN$^-$ (right) wounds. Scale bar, 500 μm. White dotted line represents dermal:hypodermal border. Right: Bar graph shows Sirius red intensity in WT WIHN$^-$ (white) and WIHN$^+$ (black) wound dermis. (**D**) Quantitative reverse transcription polymerase chain reaction (qRT-PCR) of WIHN$^-$ (white) and WIHN$^+$ (black) wound dermis at WD16 and WD22 for specified genes. Experiments used the comparative C_T method (*64*), with complementary DNAs equalized for glyceraldehyde phosphate dehydrogenase (GAPDH) or 18*S*. (**E**) Graph shows percent of cells with nuclear β-Cat in WIHN$^-$ (white) and WIHN$^+$ (black) wounds at WD18. See fig. S1 for details. (**F**) Schematic timeline highlighting the remodeling phase of healing in WIHN$^+$ (top) and WIHN$^-$ (bottom) wounds. Red bar signifies "Transition" period, i.e., completion of reepithelialization (all wounds), down-modulation of ECM production and Wnt activity, and initiation of hair neogenesis (completed by WD22) in WIHN$^+$ wounds. WIHN$^-$ wounds continue unabated production of ECM components and maintain high Wnt activity. Data are expressed as means ± SEM. **P* value is 0.05, ***P* value is 0.01, ****P* value is 0.005. *N* = number of wounds analyzed. Wounds were analyzed between WD22 and WD28 for contraction, hair follicle number.

modest immune cell compartment and a minor *Prom1*$^{+}$ population, indicative of hair follicle dermal papillae (DP) (Fig. 2, A and B, and fig. S2, A and H). In contrast, in the WIHN^{-} RNA-seq analysis (approximately 5199 cells), most myofibroblasts fell into a single cluster, no DP signatures were observed, and there was a remarkable expansion of immune cells, including macrophages and dendritic cells (DCs; Fig. 2, A and B, and fig. S2A).

Detailed examination of myofibroblast clusters under WIHN^{+} and WIHN^{-} conditions showed that both phenotypes contained three basic myofibroblast groups. Groups I and II were broadly similar in

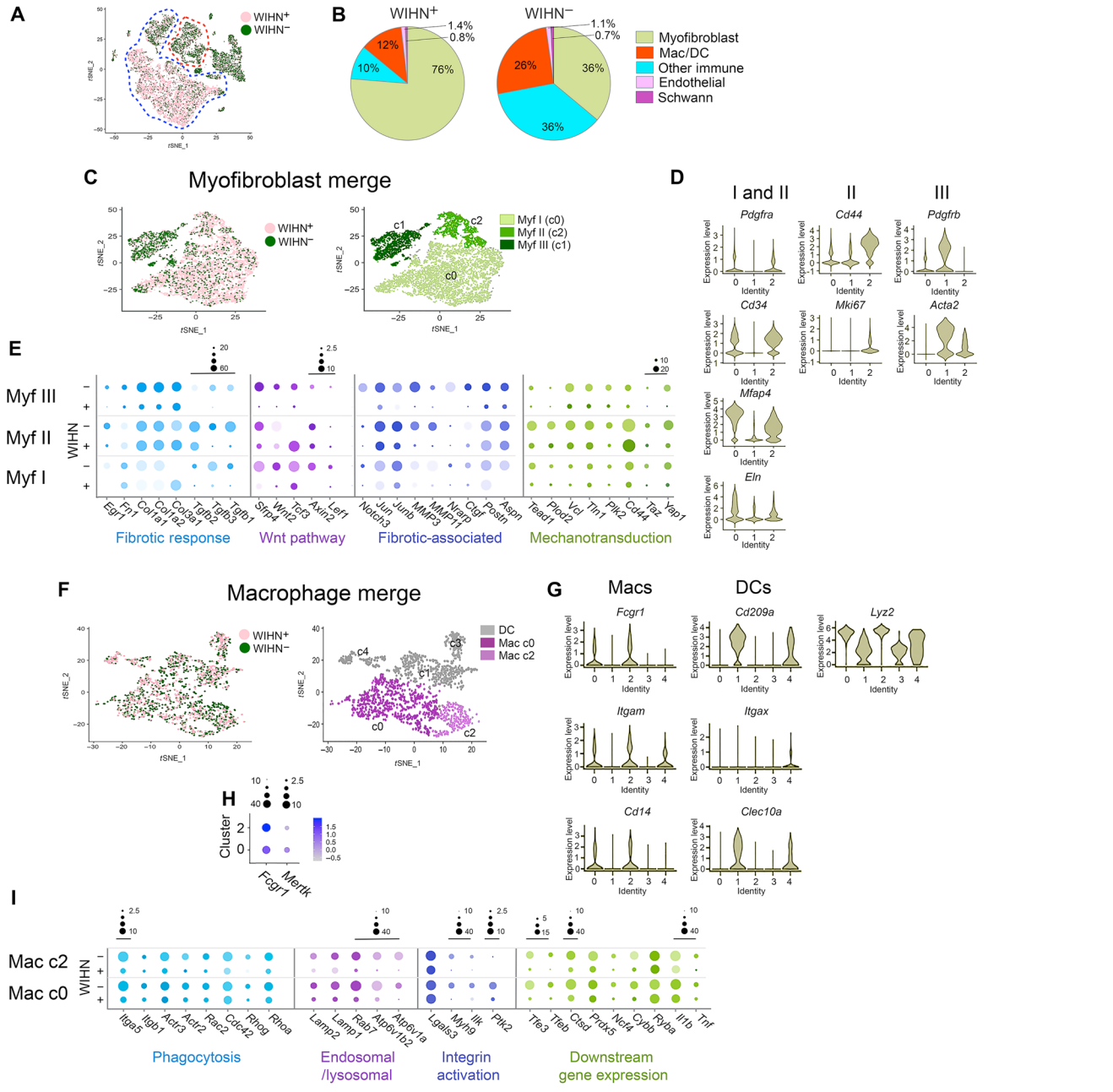

Fig. 2. Single-cell RNA-seq analysis reveals overrepresentation of fibrotic myofibroblasts and phagocytic macrophages in WD18 WIHN^{-} dermis. (**A**) Integrated whole dermis WIHN^{+} (approximately 10,587 cells, pink)/WIHN^{-} (approximately 5199 cells, green) *t*-SNE plot. Blue dotted line outlines myofibroblast clusters. Red dotted line outlines macrophage/DC clusters. (**B**) Pie charts show relative percentages of cell identities in WIHN^{+} and WIHN^{-} wounds. (**C**) Integration analysis of myofibroblast clusters only. (i) Integration *t*-SNE plot of WIHN^{+} and WIHN^{-} myofibroblasts (WIHN^{+}, pink; WIHN^{-}, green). (ii) Color blocked *t*-SNE plot shows mapped distribution of myofibroblast groups I to III. See fig. S2 for details. (**D**) Violin plots show distribution of selected genes within "merged" analysis. (**E**) Dot plots examine differential expression of selected genes in myofibroblast clusters (grouped I to III). Unless otherwise noted, expression "window" is 10 to 100. (**F**) Integration analysis of macrophage/DC clusters only. (i) Integration *t*-SNE plot of WIHN^{+} (pink) and WIHN^{-} (green) macrophages. (ii) Color blocked *t*-SNE plot with mapped distribution of macrophages and DC populations. (**G**) Violin plots showing cluster distribution of selected genes. (**H**) Dot plot shows expression of *Fcgr1* (CD64) and *MerTK* in integrated macrophage clusters c0 and c2. (**I**) Dot plots examine differential expression of selected genes in WIHN^{+} and WIHN^{-} macrophage clusters c0 and c2.

gene signatures and strongly resembled previously described myofibroblast populations with adipocyte precursor (AP) characteristics (fig. S2, A and G) (*36*–*38*). Group II also showed differential up-regulation of a variety of genes including *Cd44*, *Stmn1*, etc. and included a proliferative cluster [see table S1 for groups I to III differentially expressed gene (DEG) signatures]. Both groups differed extensively from group III, the traditionally defined $\alpha SMA^{+}SM22^{+}$ myofibroblast group (*38*).

$WIHN^{+}$ and $WIHN^{-}$ myofibroblast clusters were integrated and reclustered (Fig. 2, C to E). Featureplots identified groups I to III and the integrated *t*-distributed stochastic neighbor embedding (*t*-SNE) plot confirmed good representation of all three myofibroblast groups in $WIHN^{+}$ wound dermis, whereas most myofibroblasts within $WIHN^{-}$ dermis fell into group III (Fig. 2, C and D). To ask how myofibroblast population(s) might establish the fibrotic phenotype observed in $WIHN^{-}$ wounds, comparisons of gene expression were undertaken to look for differences in fibrosis signature [including mechanotransduction (*26*)] and Wnt activity genes. Dot plots revealed that many fibrosis-related genes examined, including Wnt-related genes *Wnt2*, *Axin2*, *Lef1*, *Sfrp4*, and *Tcf3*, were up-regulated in $WIHN^{-}$ clusters, (Fig. 2E), further supporting the conclusion that ongoing Wnt activity and up-regulation of fibrosis signature genes are characteristics of $WIHN^{-}$ wounds.

Late wound macrophages not only promote dermal remodeling and appropriate regenerative healing including hair neogenesis but also play important roles in fibrosis. Comparisons in whole $WIHN^{+}$ and $WIHN^{-}$ transcriptomes revealed that they were most significantly represented in $WIHN^{-}$ wounds (12% versus 26% respectively; Fig. 2B and fig. S2A). To identify macrophages under each condition, macrophages/DCs were subclustered and examined (fig. S3, A and E). Comparisons to Immgen databases pulled out two macrophage and three or four DC clusters from $WIHN^{+}$ and $WIHN^{-}$ wounds, respectively (fig. S3, C and G). Subclustering of $WIHN^{+}$ macrophage/DC groups also pulled out a related myofibroblast cluster (fig. S3, B to D), supporting recent work that macrophages can engender myofibroblasts upon transdifferentiation (*37*).

Featureplots of $WIHN^{+}$ macrophage clusters showed shared expression of *Csf1r*, *Fcgr1* (CD64), *Ccr2*, *Itgam* (CD11b), *Mrc1* (CD206), major histocompatibility complex (MHC) class II genes, and low *Mgl2* (CD301b), suggesting high relatedness (fig. S3D). STRING (search tool for the retrieval of interacting genes/proteins) analyses of Gene Ontology (GO), Kyoto Encyclopedia of Genes and Genomes (KEGG) pathway, and Reactome databases showed high significance for macrophage-related functions in both clusters (table S2). In contrast to macrophage clusters, DCs had expression of known DC markers such as *Cd209a*, *Cd209d*, *Itgax*, high MHC class II, and high *Mgl2* (fig. S3, D and H). Cluster 5 (c5) also had high *Siglech* and *Bst* expression, suggestive of a plasmacytoid DC phenotype.

Examination of macrophages and DCs in $WIHN^{-}$ wounds showed a very similar pattern of clustering except that representation of these subsets was greatly expanded compared to $WIHN^{+}$ wounds (Fig. 2B and fig. S3, E to H). Comparison of macrophage DEG lists revealed significant overlap in macrophage gene expression (approximately 50%; fig. S3I) and functions (table S2), suggesting that similar subsets populated both wounds. However, STRING analysis also showed that $WIHN^{-}$ macrophages exhibited phagosomal functions (table S2).

Macrophages and DCs from $WIHN^{+}$ and $WIHN^{-}$ wounds were integrated and reclustered for analysis (Fig. 2, F to I). The *t*-SNE plot and examination of conserved markers confirmed that clusters from both wounds exhibited significantly overlapping gene expression (Fig. 2G and table S3). Dot plots further confirmed macrophage identity based on *Fcgr1*/*MerTK* coexpression (Fig. 2H). As previously observed (*39*), macrophages did not conform to a strong M1 or M2 phenotype (fig. S3J). Neither *Nos2* nor *Arg1* was observed in any $WIHN^{+}$ or $WIHN^{-}$ macrophage cluster, although low expression of *Mrc2* (CD206) and *Il4ra* was common to macrophage clusters. Transcripts of known genes involved in small wound fibrosis, *PDGFc*, *Igf1*, and *Retnla* were essentially absent in all macrophage/DC (Mac/DC) populations at this time point (fig. S3K).

Because STRING analysis indicated a phagocytosis signature in $WIHN^{-}$ macrophages, integrated macrophage clusters (c0 and c2) were compared for differences in expression of phagosomal, endosomal/lysosomal, integrin activation, and phagocytosis downstream genes. $WIHN^{-}$ macrophage clusters showed significant increases in expression of almost all genes examined including expression of integrin genes *Itga5* and *Itgb1* (Fig. 2I).

These combined results indicate that WD18 $WIHN^{-}$ wounds maintain primarily group III myofibroblasts with exaggerated expression of fibrotic genes and macrophages with elevated expression of phagocytic/lysosomal machinery and ongoing phagocytosis.

Macrophage numbers are higher in $WIHN^{-}$ than in $WIHN^{+}$ wounds

To address the possibility that phagocytosis by macrophages might be involved in wound fibrosis, we first determined the macrophage number and their wound locations during the transition period (WD14 to WD16). Emerging $WIHN^{+}$ and $WIHN^{-}$ phenotypes were assessed on the basis of the correlative presence or absence of new hair placodes (lymphoid enhancer-binding factor 1 or $LEF1^{+}$) and the extent of wound contraction.

Marker expression analysis confirmed that CD64 and MERTK (tyrosine kinase protein MER) colocalized on late wound macrophages, which typically resided in the lower dermis (fig. S4). F4/80, also expressed by this population, was observed on additional cells that are likely DCs.

Macrophage numbers per wound area and total dermal percentages of macrophages were quantified by immunofluorescence and fluorescence-activated cell sorting (FACS) analysis, respectively, in wild-type (WT) $WIHN^{+}$ and $WIHN^{-}$ wounds and in wounds from $Cx3cr1^{-/-}$ mice, which lack the receptor for monocyte chemoattractant CX3CL1 (fractalkine) and are known to maintain reduced numbers of late wound macrophages (*40*). In agreement with RNA-seq data, wounds exhibiting a more regenerative healing response ($WIHN^{+}$ WT and $Cx3cr1^{-/-}$) maintained significantly fewer macrophages (35 to 50%) than those in $WIHN^{-}$ WT mice (Fig. 3, A to C, and fig. S5A). In accordance, $Cx3cr1^{-/-}$ wounds phenocopied WT $WIHN^{+}$ wounds in that they maintained reduced collagen deposition (fig. S5B), reduced mRNA levels of profibrotic genes *Col1a1* and *Tgfb1* (Fig. 3D), and reduced Wnt activity as determined by AXIN2 expression in Wnt reporter $Axin2\text{-}Lacz^{+/-}$ wounds (Fig. 3E) and exhibited significantly higher hair neogenesis associated with decreased wound contraction (Fig. 3F).

To specifically correlate late wound macrophage numbers with wound fate, we used the macrophage Fas-induced apoptosis (MAFIA) mouse model, which harbors a myeloid-specific colony-stimulating factor 1 receptor (*Csf1r*) promoter–driven AP20187 drug-inducible apoptosis cassette and green fluorescent protein (GFP) tag (*41*). A single injection of AP20187 at WD8 reduced blood monocyte numbers

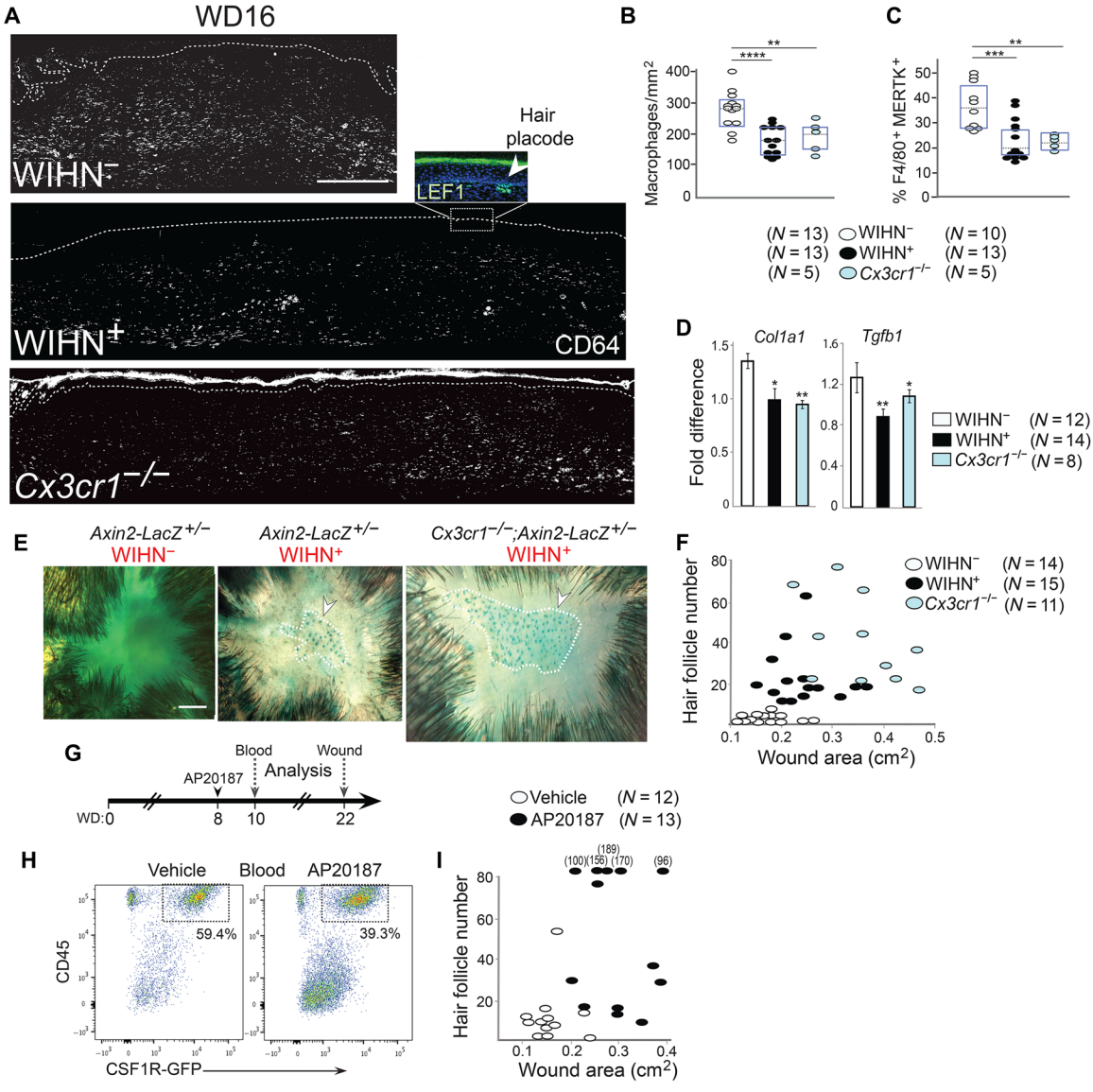

Fig. 3. Macrophage numbers in the late wound correlate inversely with regenerative WIHN$^+$ repair. (**A**) CD64 (white), LEF1 (green) in WD16 WT WIHN$^-$ (top), WIHN$^+$ (middle), and *Cx3cr1*$^{-/-}$ (lower) wounds. Inset (middle) shows LEF1$^+$ hair placode and dermal condensate (green, arrowhead). Scale bar, 500 μm. Dashed line denotes epidermal:dermal boundary. (**B** and **C**) Dot plots show macrophage numbers per mm^2 lower dermis (B) or percent per whole wound dermis by FACS analysis (C) in WD14 to WD16 WIHN$^-$ (white), WIHN$^+$ (black), and *Cx3cr1*$^{-/-}$ (blue) wounds. See fig. S5A for corresponding representative cytometric dot plots. **P* value is 0.05; ***P* value is 0.01; ****P* value is 0.005; *****P* value is 0.001. (**D**) qRT-PCR of *Col1a1* and *Tgfb1* in WT WIHN$^-$ (white), WIHN$^+$ (black), and *Cx3cr1*$^{-/-}$ (blue) wound dermis. See Fig. 1 for details. (**E**) Whole mounts of *Axin2-LacZ*$^{+/-}$ WIHN$^-$ (left), WIHN$^+$ (middle), and *Axin2-LacZ*$^{+/-}$*:Cx3cr1*$^{-/-}$ (right) wounds stained for β-galactosidase (β-Gal) activity. Circles outline regions of Axin2$^+$ hair placodes and germs. Scale bar, 1 mm. Representative of four independent experiments. (**F**) Correlative comparison of wound areas (cm^2) and hair follicle numbers in WT WIHN$^-$ (white), WIHN$^+$ (black), *Cx3cr1*$^{-/-}$ (blue) healed wounds. One-way MANOVA significance F (4,74) = 12.214, P (0.000) < 0.0005, Pillai's Trace = 0.795, η^2 = 0.398. (**G**) Timeline for injections and analyses of MAFIA wounds. (**H**) Cytometric dot plots compare percent CD45$^+$CSF1R$^+$ blood monocytes from WD10 vehicle-treated (left) and AP20187-treated (right) animals. Representative of four independent experiments. CD45$^+$CSF1R$^-$ cells in both groups are T cells. (**I**) Correlative comparison of wound area (cm^2) and hair follicle numbers in vehicle-treated (white) and AP20187-treated (right) wounds. True hair follicle numbers for wounds with >100 hair follicles are stated above dots. One-Way MANOVA F (2,22) = 21.386, P (0.000) < 0.0005, Pillai's Trace = 0.660, η^2 = 0.660.

by 33% by WD10 (Fig. 3, G and H). Examination of wounds in the AP20187-treated mice showed that they phenocopied WIHN$^+$ WT and *Cx3cr1*$^{-/-}$ wounds with significantly increased hair follicle neogenesis and decreased contraction compared to vehicle-treated animals (Fig. 3I). Thus, decreased numbers of late wound macrophages promote a regenerative process rather than fibrogenesis, and this decision is implemented after initiation of the remodeling phase.

Late wound macrophages target Wnt inhibitor SFRP4 for phagocytosis and degradation

To ask whether macrophages might be linked to chronic Wnt activity in fibrotic wounds, we first compared their location with dermal Wnt activity in *Axin2-LacZ*$^{+/-}$ wounds at WD16. Significant β-galactosidase (β-Gal) expression, indicative of strong Wnt activity, was observed in the lower dermis of WIHN$^-$ wounds, the primary location of

MERTK$^+$ macrophages (Fig. 4A, left). More detailed examination of this region revealed that Wnt-activated cells frequently resided directly adjacent to macrophages (Fig. 4B; see also Fig. 4J), suggesting that macrophages exert their influence over a short distance.

Macrophages are known to secrete Wnt ligand WNT3a and exhibit Wnt activity after tissue damage, and macrophage-secreted WNT3a is implicated as a player in both tissue regeneration and fibrosis (*23*). Examination of macrophage DEGs from both phenotypes revealed no Wnt ligand expression, and quantitative reverse transcription polymerase chain reaction (qRT-PCR) confirmed that macrophages neither expressed Wnt ligands *Wnt3a* and *Wnt2* nor did they exhibit marked Wnt activity at WD16 (Fig. 4C). As

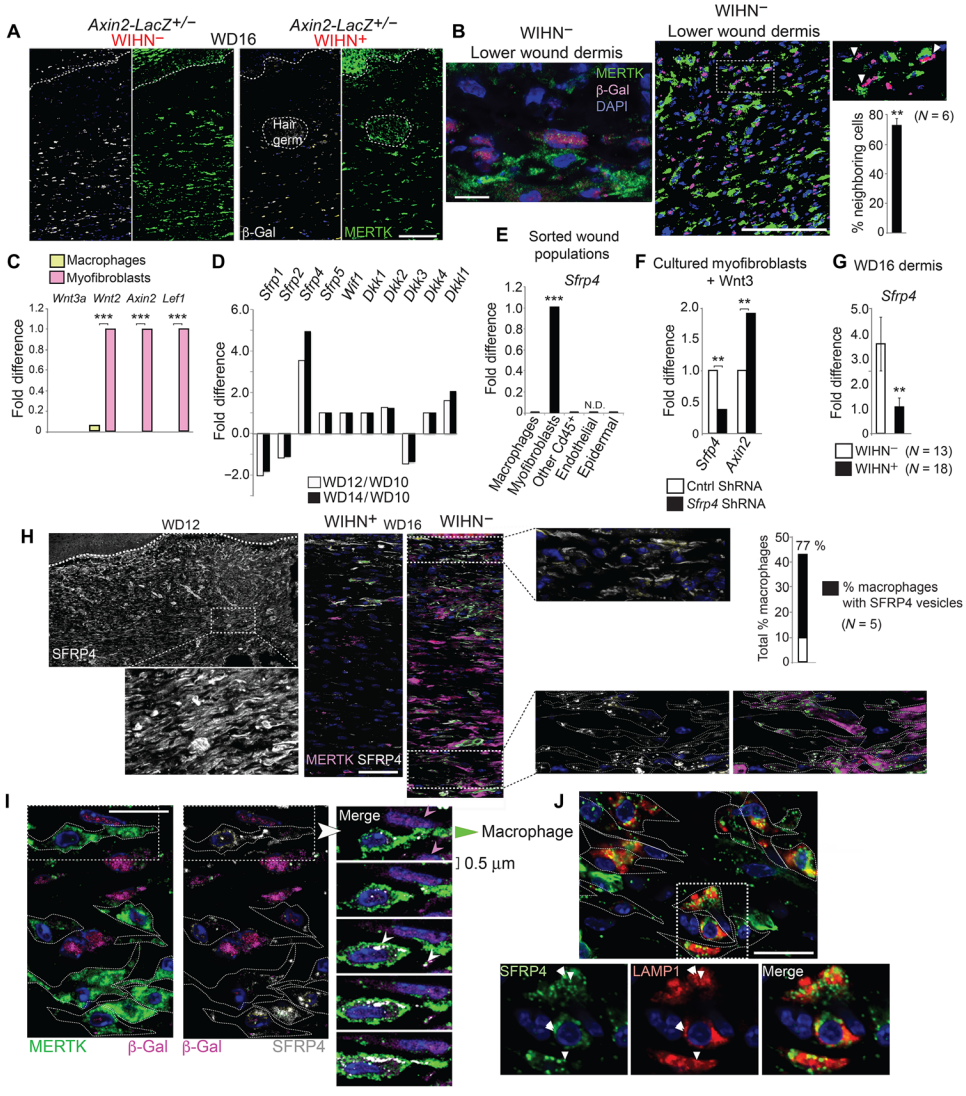

Fig. 4. Macrophages phagocytize and degrade Wnt inhibitor SFRP4 in the lower wound dermis. (**A**) β-Gal (white, left) and MERTK (green, right) localization in WD16 *Axin2-LacZ*$^{+/-}$ WIHN$^-$ (left) and WIHN$^+$ (right) wounds. Scale bar, 100 μm. Representative results from six experiments. (**B**) Left: Close apposition of β-Gal$^+$ cells (pink) and MERTK$^+$ macrophages (green) in WD16 WIHN$^-$ *Axin2-LacZ*$^{+/-}$ dermis. DAPI (4′,6-diamidino-2-phenylindole) is blue. Scale bar, 10 μm. Middle: Colocalization of macrophages (green) and β-Gal$^+$ cells (pink) in lower dermis. Scale bar, 100 μm. Right (magnification): Arrowheads point to closely associated β-Gal$^+$ cells and macrophages. Bar graph indicates percent of β-Gal$^+$ cells with closely apposing macrophages. (**C**) qRT-PCR for *Wnt3a*, *Wnt2*, *Axin2*, and *Lef1* in sorted WT wound macrophages (yellow) and myofibroblasts (pink). Combined results from three experiments. (**D**) Gene array comparison of major Wnt inhibitors between WD10 and WD12 (white) or WD10 and WD14 (black) wounds. Gene Expression Omnibus accession no. GSE46244 (*29*). (**E**) qRT-PCR of *Sfrp4* in sorted wound populations. Combined results from three experiments. (**F**) qRT-PCR of *Sfrp4* and *Axin2* in cultured Wnt-activated wound myofibroblasts transduced with lentiviral control (white) or *Sfrp4* (black) short hairpin RNAs (shRNAs). Combined results from three experiments. ***P* value is 0.01; ****P* value is 0.005. (**G**) qRT-PCR of *Sfrp4* in WD16 WT WIHN$^-$ (white) and WT WIHN$^+$ (black) wounds. (**H**) SFRP4 (white) at WD12 (left, top and bottom magnification) or WD16 (middle and right, respectively). WD16 wounds costained for MERTK (purple). Scale bar, 50 μm. In magnified panels at far right, dotted lines represent macrophage boundaries. Representative results from six experiments. Stacked bar graph (right) shows percent of total WD16 WIHN$^-$ dermal macrophages containing SFRP4 vesicles (black). (**I**) Left: MERTK (green), nuclear β-Gal (pink), and SFRP4 (white) in WD16 *Axin2-LacZ*$^{+/-}$ lower dermis. Scale bar, 10 μm. Right: Sequential slices (0.5-μm difference) of color-merged magnified region (rectangle). Pink arrowheads point to β-Gal$^+$ cells, white arrowheads point to SFRP4. Representative results from eight experiments. (**J**) Top: SFRP4 (green) and LAMP1 (red) in WD16 WIHN$^-$ lower dermis. Dotted lines represent macrophage boundaries. Bottom (magnified): Arrowsheads in left and middle panels correspond to regions of overlap. Scale bar, 10 μm. Representative results from five experiments. In (A) and (H), dotted lines denote epidermal:dermal boundary. For (C) and (E) to (G), see Fig. 1 for details.

previously shown, myofibroblasts were the primary producers of and responders to WNT2, the primary Wnt ligand in the late wound dermis (*21*).

To decipher how macrophages might promote chronic Wnt activity in WIHN$^-$ wounds, we first characterized the molecular player(s) that might down-regulate Wnt activity in WIHN$^+$ wounds. Comparison of known Wnt inhibitors from gene arrays of WD10, WD12, and WD14 wounds showed *Sfrp4* to be the only member up-regulated after initiation of dermal Wnt activity in the late wound (Fig. 4D). qRT-PCR analysis of sorted myofibroblasts confirmed RNA-seq results that *Sfrp4* is a myofibroblast product (Fig. 4E), and short hairpin RNA (shRNA) knockdown of *Sfrp4* in Wnt-activated wound myofibroblasts in vitro showed a down-modulatory role for this protein in wound Wnt signaling (Fig. 4F). In agreement with recent evidence that *Sfrp4* is a Wnt target gene (*42*), qRT-PCR confirmed RNA-seq results that mRNA levels were significantly higher in Wnt-active WIHN$^-$ wounds during late healing (Figs. 2E and 4G). Together, these results indicate that Wnt activity in myofibroblasts is modulated by SFRP4 (secreted frizzled-related protein 4) in an autocrine fashion and that unabated Wnt activity in WIHN$^-$ wounds persistently drives SFRP4 expression in an unsuccessful attempt to achieve Wnt down-modulation.

To determine SFRP4 protein localization in the healing wound, we first examined wounds at WD12, a time point when *Sfrp4* mRNA levels are elevated (see Fig. 4D). Widespread SFRP4 expression was observed in all wounds surveyed (Fig. 4H, left), in accordance with widespread dermal Wnt activity observed at this time (*22*). SFRP4 expression was then examined at WD16, when Wnt activity was substantially down-modulated in WIHN$^+$ wounds but maintained in WIHN$^-$ wounds. In accordance with Wnt activity, SFRP4 was absent from the lower dermis of WIHN$^+$ wounds but was observed in WIHN$^-$ wound dermis in Wnt-active macrophage-rich regions (Fig. 4H, center, and fig. S6A for only extracellular localization of SFRP4). Examination of SFRP4 in the WIHN$^-$ upper dermis, where residual levels could still be observed in both phenotypes, revealed a strand-like appearance along myofibroblasts and ECM, whereas in lower dermis, it showed a punctate pattern within many macrophages (Fig. 4H, right). Detailed microscopic examination of SFRP4 in the WIHN$^-$ lower dermis confirmed that, in addition to some localization within the ECM, it localized primarily to vesicles within CD64$^+$MERTK$^+$ macrophages, which adhered closely to adjacent Wnt-active cells (Fig. 4I; fig. S6, B and C; and movie S1). These SFRP4-containing vesicles sometimes costained for lysosomal marker LAMP1 (lysosomal associated membrane protein 1), suggesting targeting of SFRP4 by lysosomes for degradation (Fig. 4J).

To ask whether excessive phagocytosis of SFRP4 by macrophages might lead to the WIHN$^-$ phenotype, we inhibited phagocytosis in late wounds by injecting hemin into mice. Work by Martins *et al.* (*43*) has demonstrated that injected hemin specifically inhibits phagocytosis by macrophages and resistance to introduced bacteria in vivo. Preliminary experiments showed that hemin efficiently inhibited the ability of bone marrow (BM)–derived IL-4–polarized (regenerative) macrophages to phagocytize FN-coupled beads in vitro (fig. S7A). We then injected hemin into wounded mice after initiation of the remodeling phase (see Fig. 5A for schedule). Both vehicle [phosphate-buffered saline (PBS)]– and hemin-injected wounds underwent normal reepithelialization by WD14, and examination of wounds at WD18 showed no differences in numbers of CD45$^+$ cells, macrophages, or vasculature (fig. S7, B to F). Wounds were then examined for phagocytosis of SFRP4. Immunofluorescence analyses showed that SFRP4 vesicles were essentially absent from hemin-injected wound macrophages compared with WT WIHN$^-$ wounds despite normal macrophage numbers (Fig. 5B). Consequently, SFRP4 protein levels were significantly elevated in the wound ECM of these mice, and hemin-injected wounds exhibited hallmarks of a more regenerative healing including reduced chronic Wnt activity, reduced collagen

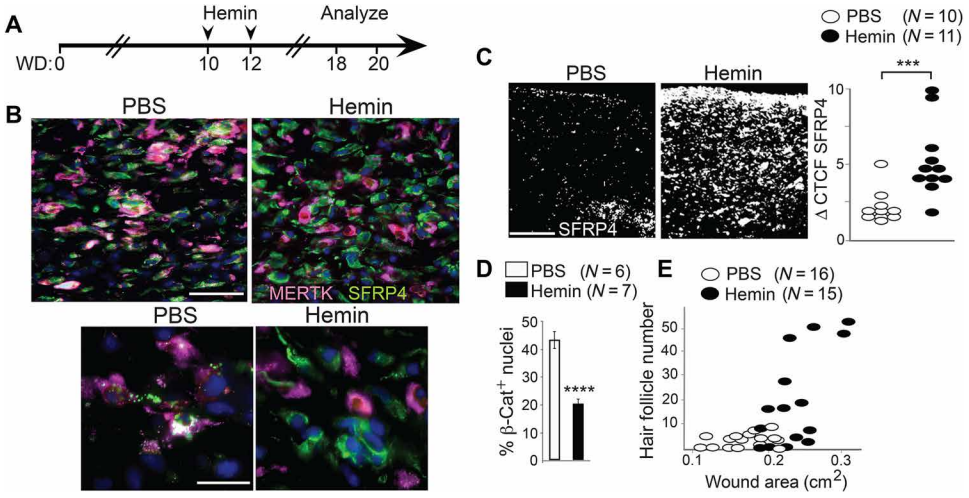

Fig. 5. Inhibition of phagocytosis in wound macrophages promotes regenerative healing. (**A**) Timeline showing hemin injection and analysis schedule. (**B**) Top: Localization of SFRP4 (green) within macrophages (purple) in lower wound dermis from PBS-injected (left) and hemin-injected (right) mice. Scale bar, 50 μm. Bottom: Magnified view of SFRP4 (green) and MERTK (purple) in PBS-injected (right) and hemin-injected (left) wound dermis. White denotes regions of colocalization. Scale bar, 25 μm. Representative of six experiments. (**C**) Left: Threshold-matched comparison of SFRP4 (white) in wounds from PBS-injected (left) and hemin-injected (right) mice. Scale bar, 100 μm. Right: Scatter plot comparing SFRP4 (corrected total cell fluorescence) in wound dermis from PBS-injected (white) and hemin-injected (black) mice. (**D**) Bar graph shows percent dermal cells with nuclear β-Cat localization in PBS-injected (white) and hemin-injected (black) wounds. (**E**) Correlative comparison of healed wound surface areas (cm^2) and hair follicle numbers in PBS-treated (white) and hemin-treated (black) wounds. One-way MANOVA significance F (2,28) = 10.658, P (0.000) ≤ 0.005, Pillai's Trace = 0.432, η^2 = 0.432. Data are expressed as means ± SEM. ***P value is 0.005, ****P value is 0.001.

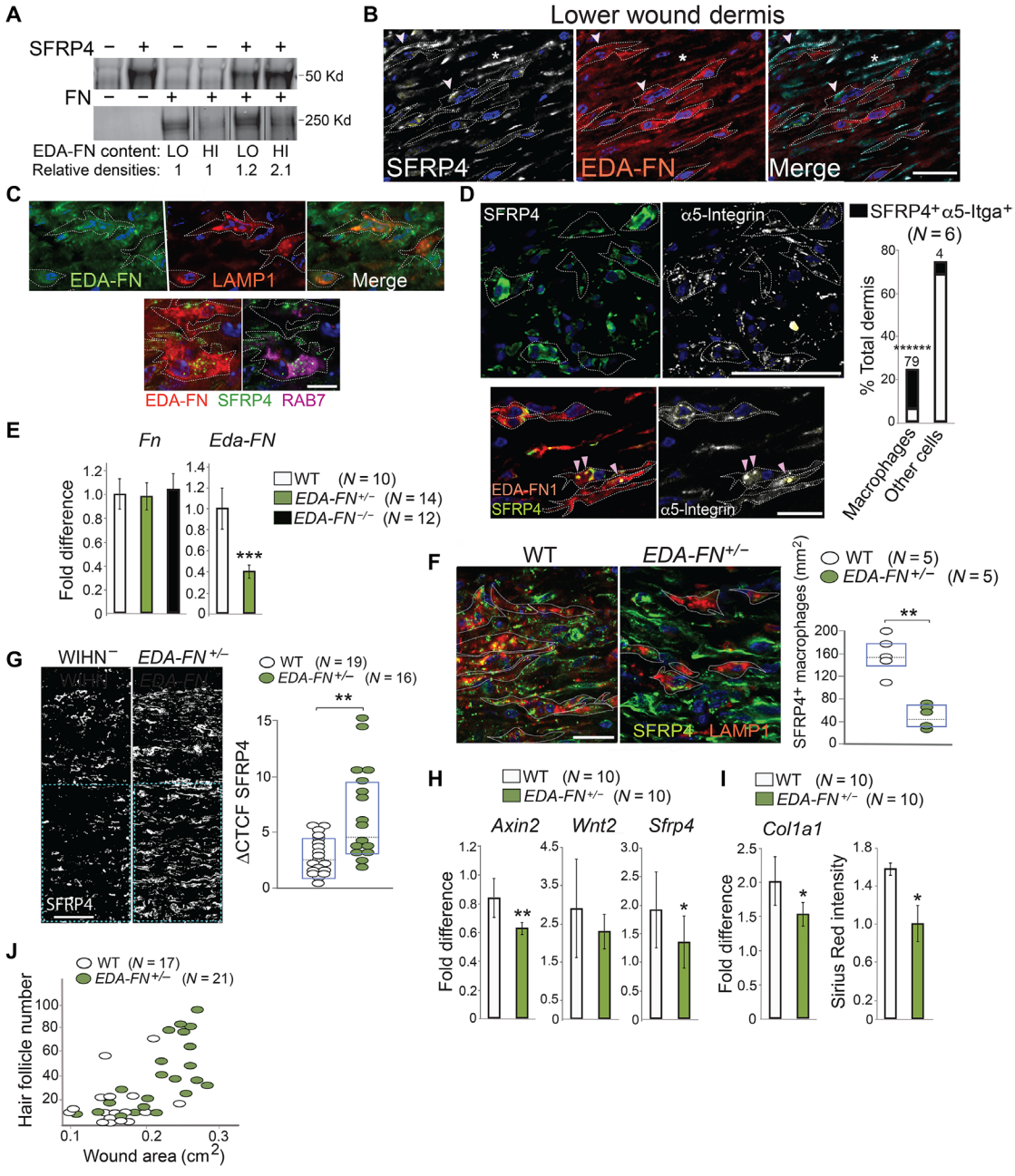

Fig. 6. Extracellular EDA-FN acts as a bridge for integrin-mediated phagocytosis of SFRP4. (**A**) Western blot of pull-down of cellular FN containing high (HI) or low (LO) EDA concentrations with SFRP4-bound beads. Protein molecular weights at the left. Relative densities are indicated. See fig. S8A for details. Representative of three independent experiments. (**B**) Localization of SFRP4 (left) on EDA-rich strands (middle) in ECM (*) and macrophages (arrowheads) in lower dermis. Scale bar, 10 μm. Representative of six independent experiments. (**C**) Top: EDA-FN (green, left), LAMP1 (red, center), merge (right) in lower wound dermis. Scale bar, 10 μm. Bottom: MERTK$^+$ macrophages (dotted lines) stained for SFRP4 (green) and EDA-FN (red, left) or RAB7 (purple, right) in lower dermis. Scale bar, 5 μm. Representative of nine independent experiments. (**D**) Top: SFRP4 (green) and α5-integrin (white) colocalization in WD16 lower dermis. See fig. S8D for details. Scale bar, 50 μm. Stacking bar graph shows percent (above bar) of total macrophages (left) or other cells (right) positive for α5-integrin + SFRP4 (black). Four percent overlap in other cells was predominantly vasculature. Bottom: Colocalization of EDA-FN (red), SFRP4 (green, left), α5-integrin (α5-integrin, white, right) in WD16 wound lower dermis. Arrowheads point to colocalization. Representative of six independent experiments. (**E**) qRT-PCR of WD16 WT (white), *EDA-FN*$^{+/-}$ (green), and *EDA-FN*$^{-/-}$ (black) wounds for total *Fn1* (left) and *Eda-FN* (right). (**F**) Left: SFRP4 (green) and LAMP1 (red) colocalization in WT (left) and *EDA-FN*$^{+/-}$ (right) lower wound dermis. Scale bar, 10 μm. (See fig. S9E for LAMP1 and MERTK colocalization in these images). Right: Scatter plot shows relative number of SFRP4 vesicle–bearing macrophages/mm^2 in WD16 WT (white) versus *EDA-FN*$^{+/-}$ (green) wounds. (B to D and F) Dotted lines represent macrophage boundaries. (**G**) Left: Threshold-matched comparisons for SFRP4 in WD16 WT WIHN$^+$ (left), WT WIHN$^-$ (middle), and *EDA-FN*$^{+/-}$ (right) wounds. Scale bar, 50 μm. Right: Quantitation of SFRP4 (ΔCTCF) in WT (white) and *EDA-FN*$^{+/-}$ (green) wounds. (**H** and **I**) qRT-PCR of WT (white) and *EDA-FN*$^{+/-}$ (green) wound dermis for indicated genes. (I) Right: Sirius red intensity in WT (white) and *EDA-FN*$^{+/-}$ (green) wounds. (**J**) Correlative comparison of wound areas (cm^2) and hair follicle numbers in WT (white) and *EDA-FN*$^{+/-}$ (green) wounds. One-way MANOVA significance $F(2,36) = 6.383$, P (0.004) < 0.005, Pillai's Trace = 0.262, $\eta^2 = 0.131$. For (E), (H), and (I), see Fig. 1 for details.

deposition, and reduced contraction correlating with increased hair neogenesis (Fig. 5, C to E, and fig. S7G).

These combined results suggest that high numbers of macrophages can prevent Wnt down-modulation in the wound and promote a fibrotic WIHN$^-$ phenotype through persistent degradation of an important Wnt inhibitor, SFRP4, and that inhibition of this macrophage function can reverse this phenotype.

Phagocytosis of SFRP4 by late wound macrophages is integrin dependent and requires association with EDA-FN

We next asked how macrophages phagocytize SFRP4. Related SFRP family member SFRP2 can associate with FN (*44*), a known mediator of bacterial or apoptotic cell phagocytosis by macrophages (*29*). We therefore asked whether SFRP4 might require association with FN for phagocytosis, and we focused on extra domain A (EDA)–FN, the predominant FN splice variant in wound dermis (*45*).

Protein pull-down experiments showed that SFRP4 associated preferentially with EDA-rich FN compared to cellular FN containing other splice variants (Fig. 6A and fig. S8A for details). Analysis of frozen wound sections showed localization of SFRP4 to EDA-FN strands in the ECM (Fig. 6B) and many EDA-FN–containing vesicles within wound dermal macrophages, some of which localized to LAMP1$^+$ lysosomes (Fig. 6, B and C). SFRP4 colocalized with EDA-FN within some vesicles in wound macrophages and both localized to RAB7$^+$ late endosomes (Fig. 6C). In vitro phagocytosis studies showed that BM-derived IL-4–polarized macrophages could ingest and target SFRP4-bound EDA-FN–coupled beads to LAMP1$^+$ lysosomes (fig. S8B). EDA-FN can also interact with Toll-like receptor 4 (TLR4), and this interaction, in association with integrins on fibroblasts, can drive fibrosis (*46*, *47*). *Tlr4* mRNA levels were reduced by WD12 (fig. S8C), and single-cell RNA-seq DEG lists of WIHN$^+$ and WIHN$^-$ dermal populations did not bring up either *Tlr4* or *Elane* (elastase-2), the enzyme required to expose the cryptic EDA domain for binding, in any wound population (*48*). Violin plots confirmed very low to no expression of *Tlr4* in both myofibroblast and macrophage/DC populations, and dot plots of integrated myofibroblasts showed that when *Tlr4* could be detected, its expression was often comparable or higher in WIHN$^+$ clusters (fig. S8C). Together, these results indicate that the SFRP4:EDA-FN complex can be phagocytized and targeted for degradation by wound macrophages and that TLR4:FN interactions do not play a role in fibrosis during this period in this model.

As integrins are FN receptors and are required for FN-mediated phagocytosis (*29*), we studied their role in phagocytosis of the SFRP4:EDA-FN complex. In vivo examination revealed frequent colocalization of α5-integrin, an established FN receptor (*49*) with SFRP4 specifically within wound macrophages (Fig. 6D, top, and fig. S8D), and detailed analyses confirmed colocalization of both SFRP4 and EDA-FN with either α5-integrin or its binding partner β1-integrin within wound macrophages (Fig. 6D, bottom, and fig. S8E). In vitro pretreatment of BM-derived IL-4–polarized macrophages with blocking anti–β1-integrin antibody completely abrogated phagocytosis of EDA-FN beads (fig. S8F). Together, these observations suggest that EDA-FN acts as a bridge to target SFRP4 for integrin-mediated phagocytosis by macrophages.

We hypothesized that if EDA-FN targets SFRP4 for phagocytosis, then loss of this protein should result in a wound phenotype similar to that observed in phagocytosis-deficient hemin-treated mice (see Fig. 5). To address this, we examined wounds from *EDA-FN*$^{-/-}$ and *EDA-FN*$^{+/-}$ mice. Wounds from *EDA-FN*$^{-/-}$ mice had no expression of EDA-FN and maintained high levels of compensatory EDB-FN (Fig. 6E and fig. S9, A and B). Compared to WT, *EDA-FN*$^{-/-}$ wounds revealed a distinct nonfibrous pattern of FN deposition and very little FN:SFRP4 colocalization, further confirming that SFRP4 preferentially binds EDA-FN (fig. S9B and see Fig. 6B for comparison).

EDA-FN$^{-/-}$ mice have been shown to exhibit some wound healing defects (*50*), prompting us to use *EDA-FN*$^{+/-}$ mice for our studies. *EDA-FN*$^{+/-}$ wounds had significantly reduced EDA-FN mRNA and protein levels (Fig. 6E and fig. S9A), although wounds healed completely, without significant delay and exhibited normal dermal remodeling (fig. S9, A to C). Further, *EDA-FN*$^{+/-}$ wound dermis maintained normal numbers of late wound macrophages with normal capacity to phagocytize EDA-FN–coupled beads (fig. S9, C and D).

To ask whether reduced expression of EDA-FN might affect SFRP4 turnover by wound macrophages, comparisons of *EDA-FN*$^{+/-}$ and WT wounds were undertaken. In *EDA-FN*$^{+/-}$ wounds, SFRP4 localization within macrophages, and specifically, within LAMP1$^+$ lysosomes, was significantly reduced (Fig. 6F). In agreement with this finding, increased SFRP4 protein levels were found in the ECM of *EDA-FN*$^{+/-}$ wound dermis (Fig. 6G). *EDA-FN*$^{+/-}$ wounds also exhibited reduced Wnt activity (Fig. 6H), reduced collagen transcription and protein expression (Fig. 6I and fig. S9A), reduced wound contraction, and significantly higher hair neogenesis than WT littermates (Fig. 6J), all indicative of a more regenerative fate. Together, these results show that *EDA-FN*$^{+/-}$ wounds phenocopy phagocytosis-deficient wounds, indicating that EDA-FN is important for SFRP4 turnover by wound macrophages.

EDA-FN and SFRP4 expressed in human hidradenitis suppurativa wound dermis are targeted by macrophages for phagocytosis

Hidradenitis suppurativa (HS) or acne inversa is a common chronic skin disorder characterized by recurring follicular occlusions and inflammation, leading to recurring localized wounding and subsequent fibrotic scarring (see fig. S10A for a representative diagram of these regions in HS skin) (*51*). Although macrophages are known important contributors to this disease, their role has not been established (*52*).

In agreement with previous observations of granulation tissue formation in this disease, we found that regions i and ii (see fig. S10A) contained cells expressing EDA-FN, SFRP4, and αSMA, whereas long-standing fibrotic regions from the same patient exhibited high levels of collagen but like normal skin, low levels of these proteins (figs. S10, B and C, and S11A). As observed in mouse wounds, EDA-FN frequently colocalized with SFRP4 in new wounds, indicating their close association (fig. S11B).

Immune infiltrates (region i) and adjacent dermis (region ii) were rich in CD68$^+$ macrophages, many with vesicles containing SFRP4 (fig. S10D). Close examination of these vesicles showed occasional colocalization of SFRP4 with EDA-FN and LAMP1 (fig. S10E), suggesting that human wounds, such as mouse wounds, target SFRP4 for EDA-FN–mediated phagocytosis and subsequent degradation. Last, nuclear β-Cat localization remained high in immune infiltrate (region i), adjacent dermis (region ii), and distant fibrotic regions (fig. S10, F and G), indicating chronic Wnt activity throughout HS-damaged skin. qRT-PCR comparisons of HS and normal dermis confirmed high Wnt activity and increased expression of fibrogenic genes (fig. S10H).

These results highlight the notable similarities between mouse and human wounds and suggest that phagocytosis of SFRP4 by

macrophages may be a common mechanism for fibrotic skin wound healing in these species.

DISCUSSION

In this work, we show that late stage wound macrophages phagocytize and degrade wound Wnt inhibitor SFRP4 to drive chronic Wnt activity to promote fibrogenesis over regeneration. ECM component EDA-FN binds SFRP4 and acts as a bridge for its engulfment (model, see fig. S12). Obstruction of phagocytosis is alone sufficient to alter wound fate from fibrotic to a more regenerative response, indicating that this mechanism is a major contributor to skin fibrotic repair and may have broader relevance than to skin wound healing alone. Here, we show that the key component is an FN bridge, hypothetically capable of binding many different substrates for phagocytosis. Thus, other environmental mediators might also be targets of this mechanism. In addition, ECM components such as collagen, which are subject to mannose receptor–mediated remodeling by macrophages (*31*), might serve as alternative tethering components.

Several important questions remain. First, what earlier healing events determine the disparate macrophage density observed in WIHN$^+$ and WIHN$^-$ wounds? Results by Kasuya *et al.* (*35*) suggest that regenerative macrophages may be present by WD7. Inflammation is an early event that sets the stage for all later healing, and the extent of inflammation likely affects the ultimate wound fate. However, whether this impact is reflected through early recruitment of large numbers of macrophages that later contribute directly to remodeling or to later events, which may drive de novo migration of macrophages into the wound, remains unknown. Second, RNA-seq analyses revealed not only the presence of high numbers of macrophages in WIHN$^-$ wounds but also their increased transcription of phagosomal/lysosomal genes. Recent work has shown that phagocytosis can augment subsequent phagocytosis in a receptor-independent manner through translocation of transcription factor TFEB (transcription factor EB) to the nucleus and up-regulation of lysosomal genes such as *Ctsd* (*53*). Here, we show that both *TFEB* and *Ctsd* transcripts are up-regulated in WIHN$^-$ macrophages. We postulate that large numbers of macrophages initiate widespread loss of SFRP4 to prolong Wnt activity. Once this cascade has begun, increased production of fibrosis signature protein FN1 would provide additional fodder for uptake by an increasingly efficient phagocytic population, thus further promoting an autofeedback loop for continued Wnt activity and fibrotic repair.

Multiple myofibroblast subsets, including PDGFRa$^+$ AP-type (groups I and II in this study) and PDGFRb$^+$ classical myofibroblasts (group III in this study), have been identified in lung, skin, adipose tissue fibrosis (*36*–*38*). The importance of AP-type myofibroblasts to fibrosis in adipose tissue has been shown (*38*) and, in small skin wounds, which invariably heal in a scarring phenotype, AP-type myofibroblasts contribute to skin fibrotic repair (*36*). In unbiased transcriptome comparisons of bleomycin-induced fibrosis versus normal lung, Xie *et al.* (*54*) observed expansion of multiple PDGFRa$^+$ and PDGFRb$^+$ myofibroblast populations and described a previously unidentified PDGFRb$^+$ subset with elevated expression of *Notch3* and fibrosis signature genes, which they concluded might provide a true lung fibrogenic myofibroblast phenotype. Our single-cell RNA-seq comparisons also revealed fibrogenic PDGFRa$^+$ (groups I and II) and PDGFRb$^+$ (group III) subtypes in the WIHN$^-$ wound, although there was preferential screwing toward group III. All groups exhibited elevated fibrosis signature genes. These results support the hypothesis that both classical and AP-type myofibroblasts contribute to fibrosis in skin wound healing and that classical myofibroblasts may prove the most important for long-term fibrosis maintenance.

In small skin wounds, F4/80$^+$CD206$^+$CD301b$^+$ myeloid cells were shown to express IGF1 and PDGFC. Further, these cytokines induced proliferation of APs, promoting their fibrogenic involvement (*36*). In other studies, alternatively activated macrophages have been shown to secrete RELM-α promoting profibrotic collagen cross-linking (*26*). In our studies, WIHN$^-$ macrophage/DC populations had slightly elevated *Igf1* within a DC subset and no expression of either PDGFC or RELM-α. These differences in results likely reflect the wound type (small versus large), timing, and/or the possibility that some of these proteins may be long lived in the ECM and require little new transcriptional activity for their continued functioning. In the WIHN wound model, we found up-regulated phagocytosis by wound CD64$^+$MERTK$^+$ macrophages in fibrotic wounds. Abrogation of this function resulted in a more regenerative repair, demonstrating that phagocytosis is a keystone mechanism of fibrosis in this model.

Expanding on the demonstration that macrophage-elicited tumor necrosis factor (TNF) promotes hair regeneration after plucking (*55*), Wang *et al.* (*34*) recently reported the same requirement for hair neogenesis after wounding. In support of this, Chen *et al.* (*55*) showed that macrophage-elicited TNF can promote Wnt ligand secretion by epidermal cells after hair plucking. As epidermal Wnt expression is a requisite for hair neogenesis (*33*), TNF production during reepithelialization could provide a potentially important pathway to placode induction. Our single-cell RNA-seq analysis revealed low expression of *TNF* by macrophages at WD18 in regenerative wounds and slightly increased expression in fibrotic wounds. Given the remarkable plasticity of macrophages in response to their environment, it is likely that their gene signatures change rapidly, as wound dermis transforms during the healing process making it plausible that TNF levels 3 to 4 days earlier may indeed be elevated in WIHN$^+$ wounds.

Wnt activity has been reported to affect the TGFβ pathway in a variety of scenarios, including wounding (*13*, *15*). Our results suggest that elevated Wnt activity may directly affect TGFβ signaling for chronic activation of both and that sustained high Wnt activity precedes up-regulation of TGFβ and its targets by at least several days, thus making it an earlier benchmark for the cross-talk between Wnt and TGFβ pathways in fibrogenesis.

How fibrogenesis in wound healing precludes hair neogenesis remains unclear. Recently, Rognoni *et al.* (*56*) compared small wounds from young and adult mice, which result in hair neogenesis or scarring, respectively, and found that increased Wnt activity in older wounds correlated with loss of hair neogenesis. This finding supports the hypothesis that high chronic Wnt precludes hair neogenesis. High Wnt activity in fibrogenic wounds might promote fibrogenic over DP-forming programs in myofibroblasts, or because dermal Wnt activity precedes and is necessary for subsequent epidermal Wnt activation (*21*, *57*), chronic dermal Wnt might indirectly affect placode initiation in the overlying epidermis. Because overexpression of SHH can override some aspects of the fibrotic wound environment to permit hair neogenesis suggests that it may also override chronic Wnt activity or its impact in small wounds (*58*). Last, hair neogenesis is absent from adult small wounds and only observed in the center of large wounds, suggesting a paracrine inhibitory effect by the surrounding unwounded environment. Therefore, wound

contraction alone might be sufficient to place WIHN$^-$ epidermis and upper dermis closer to these external inhibitory influences, including Wnt ligands.

In mammals such as humans and rats, hair neogenesis is a very rare occurrence following wounding, likely reflecting rapid and sustained inflammatory responses to manage infection and augment rapid wound closure at the cost of a more regenerative response. In humans, SFRP4 expression has been associated with fibrotic skin diseases such as psoriasis and Dupuytren's disease (*59*, *60*). Here, we show that extensive degradation of SFRP4 by macrophages in immunologically active zones in HS skin correlates with chronic Wnt activity and fibrogenesis, conditions that are also common to Dupuytren's syndrome (*60*). These results underscore the importance of modulating Wnt activity in wounding responses to chronic fibrotic skin disorders like HS and Dupuytren's syndrome, surgery, radiotherapy, and possibly tumorigenesis and suggest that modulation of regenerative macrophage activity in particular may provide novel therapeutic avenues for wound treatment.

MATERIALS AND METHODS

Study design

The purpose of this study was to identify and understand the mechanisms used by late wound macrophages to affect skin regeneration and fibrosis. All animal protocols were reviewed and approved by the French Research Ministry and Institutional Animal Care and Use Committee. Sample size was determined from previous experimentation, and end points for data collection were reached when statistical significance was achieved or for immunofluorescence experiments not dependent on statistical analyses, at least three comparable examples were obtained. All animal studies were conducted on 3 to 30 biological replicates. To avoid bias, all animals were housed identically, and WT littermates were maintained with and compared to treated or genetically altered mice at ages ranging from 6 to 8 weeks. No formal randomization or blinding was performed, but results were confirmed by at least two independent experiments. See figure legends for replicate sizes. Control and HS skin was collected from male and female patients following consent of the individuals and approval by the Ethics Commission of the Medical Faculty of the University of Leipzig.

Human skin used in these studies

Human skin samples were obtained after informed consent from patients undergoing reconstructive surgery procedures (controls) and from patients receiving surgical removal of stage 2 and 3 HS lesions with the approval of the Ethics Commission of the Medical Faculty of the University of Leipzig (Az. 428/16-ek). HS material was collected from surgical excisions containing lesioned skin only. The samples were collected immediately after surgery and embedded in optimal cutting temperature compound (OCT), frozen, and kept at −80°C until cryosectioning or transferred to RNAlater (Sigma) and frozen at −80°C for later qRT-PCR analyses.

Mice used in these studies

The transgenic and knockout mice used in these studies include *Cx3cr1*$^{-/-}$ mice (JAX stock 005582), *AXIN2-LacZ* reporter mice (JAX stock 009120), MAFIA mice (JAX stock 005070), *EDA-FN*$^{-/-}$, and *EDA-FN*$^{+/-}$ mice (European Mouse Mutant Archive repository). *EDA-FN*$^{-/-}$ mice were further backcrossed onto a C57BL/6J background to achieve an *N* of 10 to 11. C57BL/6J control mice were purchased from Charles River Laboratories, France.

Wounding protocol

Full thickness excision of skin was performed on the backs of adult 6- to 8-week-old mice under isoflurane anesthesia as previously described (*35*). Mice received 1.2 cm × 1.2 cm full thickness excision wounds on the lower back in all experiments. Animals received analgesic buprenorphine before surgery and 8 and 24 hours later to ameliorate pain. All animal protocols were reviewed and approved by the French Research Ministry and Institutional Animal Care and Use Committee (Bioproj APAFIS#2673-2015111317111206). Wounds typically healed completely within 14 days with extensive dermal remodeling and complete reepithelialization. Wounds from all transgenic and knockout mouse lines healed completely and without extensive delay (no more than 48 hours). In phagocytosis inhibition experiments, hemin (Sigma 51280) was prepared and injected as previously described (*46*) into wounded mice at WD10 and WD12. In all experiments, mice were maintained in microisolator cages to reduce the risk of infection.

Tissue treatment, hair neogenesis, and wound size analyses

Healed skin was taken 2 to 14 days (WD16 to WD28) after reepithelialization, and epidermis and dermis were separated using 20 mM EDTA or dispase. To determine the number of hair placodes in WD16 skin, epidermis was stained with anti–LEF1-GFP antibody, and placodes were recorded throughout the entire epidermis using a Leica TCS SP8 confocal microscope for tiling acquisition, followed by analysis with ImageJ software. Dermis was dissociated as previously described (*22*), and cells were analyzed by FACS, qRT-PCR, or cell sorting and subsequent qRT-PCR analyses (see below). Wounds were photographed using a Leica MZ6 stereomicroscope fitted with a high-resolution digital camera, and digital images were analyzed for surface area using ImageJ software. New hairs were counted by direct microscopic visualization, and numbers were verified by dermal NBT/BCIP (nitro blue tetrazolium/5-bromo-4-chloro-3-indolyl phosphate) staining as previously described (*35*).

Whole-mount assays to detect β-Gal activity

To detect β-Gal activity in *AXIN2-LacZ*$^{+/-}$ wounds, tissue was treated as previously described (*22*).

Antibodies used in these studies

For macrophage identification and dermal sorting, the following antibodies were used: anti-F4/80 (clone BMB, eBioscience), anti-CD64 allophycocyanin (APC; X54-5/7.1, BioLegend), anti-MERTK biotin (R&D Systems BAF591), anti-CD301b Alexa Fluor 647 (LOM-8.7, BioLegend), anti-CD206 APC (C068C2, BioLegend), anti-CD45 (clone 30-F11, BD Biosciences), anti-CD31 (clone MEC 13.3, BD Biosciences), anti–CD11b-APC (clone ICRF44, eBioscience), anti–CD209-AF647 (9E9AB, BioLegend), and anti–CD68-fluorescein isothiocyanate (Y1/82A, BioLegend). For hair placode identification, the following antibodies were used: LEF1 (Cell Signaling C12A5). To detect ECM proteins, the following antibodies were used: SFRP4 monoclonal (Abcam EPR9389) and SFRP4 polyclonal (PA5-52679, Thermo Fisher Scientific); FN: Rabbit polyclonal (Abcam ab23750), EP5 (MA1-12597, Thermo Fisher Scientific), EDA-FN clone IST-9 (Abcam ab6328), and anti-FN biotin (Abcam ab6584); Cola1a: Rabbit polyclonal (PA5-29569, Thermo Fisher Scientific). Anti–β-Cat

(Abcam ab6302) and anti–β-GAL (Abcam ab9361) were used for Wnt activation analyses. To detect integrins and intracellular trafficking vesicles the following antibodies were used: β1-integrin (HMβ1-1, BioLegend), α5-integrin (5H10.27, Invitrogen), RAB7 (Abcam EPR7589), and LAMP1 (1D4B, BioLegend). LEAF Purified anti-mouse/rat CD29 antibody (HMβ1-1, BioLegend 102210) was used for phagocytosis assays.

Phagocytosis assays

Generation of BMDM (bone marrow-derived macrophage)–derived IL4-polarized (M2) macrophages: BM-derived monocytes from WT or *EDA-FN*$^{+/-}$ mice were obtained by flushing BM from adult WT mouse femora and tibias, followed by removal of red blood cells with ammonium chloride (07850, STEMCELL), filtration through a 70-μm-mesh filter (Becton Dickinson), and incubation for 3 hours in Iscove's modified Dulbecco's medium (IMDM) GlutaMAX (31980, Thermo Fisher Scientific) supplemented with 10% fetal bovine serum (Gibco), 1% penicillin-streptomycin (Life Technologies), and 150 μM monothioglycerol (Sigma-Aldrich). Nonadherent cells, seeded at a density of 3×10^4 cells/ml, were cultured in IMDM medium containing mouse CSF (25 ng/ml; 130-101-705, Miltenyi Biotec) for 7 days, changing medium every 2 days. From days 7 to 8, medium was supplemented with mouse IL-4 (10 ng/ml; Miltenyi Biotech) to facilitate differentiation of monocytes into macrophages.

Coupling of EDA-FN to beads: FNnb (EDA-FN, see fig. S7A) was coupled to Fluoresbrite Carboxylate YG 1.0-μm microspheres (Polysciences, catalog no. 15702) using the PolyLink Protein Coupling Kit (Polysciences, catalog no. 24350-1), according to the manufacturer's instruction. The extent of association was determined by cytofluorographic analyses. For studies examining SFRP4 phagocytosis, a 1:1 ratio of recombinant SFRP4 protein (1827-SF-025, R&D Systems) to FN bound to beads was incubated with FN-bound beads overnight and extent of association determined by cytofluorographic analyses.

Phagocytosis assay: Differentiated IL-4–polarized macrophages were preincubated with or without 3, 10, 15, and 30 μM hemin (Sigma 51280) for 30 min as previously indicated (*61*) or with LEAF Purified anti-mouse/rat CD29 antibody (20 μg/ml; HMβ1-1, BioLegend) or with concanamycin A (10 μM, Sigma C9705; for colocalization of FN, SFRP4, LAMP1 studies) (*61*) for 1 hour, followed by addition of FN-coupled beads, SFRP4-bound FN-coupled beads, or uncoupled beads for 1 hour at 37°C. Cells were then fixed with 4% paraformaldehyde and treated with anti-FN antibody-biotin (Abcam ab6584), followed by secondary antibody and analyzed by cytofluorography (Fig. 5A). Loss of binding to anti-FN antibody indicated that beads were internalized (*61*). For SFRP4 studies (Fig. 5B), fixed cells were analyzed for intracellular SFRP4 and LAMP1 as described for other immunofluorescence analyses (see above).

Immunofluorescence, Sirius red staining, and intensity quantitations

Tissue, flash frozen in OCT at −80°C, was cryosectioned into 12- to 14-μm-thick sections, and sections were fixed with 4% paraformaldehyde as previously described (*62*). For examination of extracellular and membrane proteins, sections were preblocked in PBS containing 1% bovine serum albumin (BSA), 1:10 anti-mouse CD16/CD32 Fc block (eBioscience), and then stained with the appropriate antibodies in 1% BSA/PBS/Fc block for 2 hours at 4°C followed by fixation. To further visualize internal antigens, sections were then incubated overnight with the appropriate antibodies in PBS containing fish gelatin and saponin, followed by fixation (*62*). To identify nuclear localization of β-Cat, fixed sections were first permeabilized with 0.3% Triton X-100, followed by incubation with anti–β-Cat antibody (Abcam ab6302) in saponin block. All sections were mounted with Vectashield DAPI (4′,6-diamidino-2-phenylindole; Vector Laboratories, H-1200) and examined using a white light TSC SP8 Leica scanning confocal microscope. Sirius Red and fluorescence intensities (ΔCTCF) in threshold-matched images were determined using ImageJ.

FACS analyses and cell sorting for qRT-PCR

The basic staining protocol for sorting of wound populations was undertaken as previously described. Briefly, dissociated wound dermal cells were stained for CD45, CD64, CD31, and propidium iodide to exclude dead cells. Gated populations were defined as CD45$^+$CD64$^+$ macrophages, CD45$^+$CD64$^-$ lymphocytes (including T cells, B cells, etc.), CD45$^-$CD31$^+$ endothelial cells, and all other CD31$^-$CD45$^-$ cells as myofibroblasts. FACS analyses were undertaken using a FACSCanto A or LSRii and cell sorting using FACSAria and FACSDiVa software. Data were analyzed using FlowJo software.

Single-cell RNA-seq of WIHN$^+$ and WIHN$^-$ wound dermis

WD18 epidermis and dermis were separated, and epidermis were stained for LEF1 to assay for hair placodes. WIHN$^+$ and WIHN$^-$ wounds were defined on the basis of the appearance of placodes and on increased wound size. Approximately 7 to 10 wounds of each phenotype were combined, dermal cells were released by collagenase treatment (Worthington Labs) and filtered, and dead cells and debris were removed using the MACS Live-Dead kit (Miltenyi Biotec). Cells were subjected to 10× Genomics Chromium Single-Cell Platform manipulation, followed by sequencing using Illumina HiSeq 4000 system, and then results were run through Cell Ranger pipeline software for sequence alignment and basic filtering. The following expression matrices were used: WIHN$^+$: capture of approximately 10,500 dermal cells with average read depth of approximately 41,000 reads per cell across 19,000 genes with 3200 median unique molecular identifiers; WIHN$^-$: capture of approximately 5500 dermal cells with average read depth of approximately 70,000 reads per cell across more than 17,000 genes with over 2400 median unique molecular identifiers. Expression matrices underwent filtering, normalization, scaling, principal components analysis, and subsequent *t*-SNE analysis using Seurat packages (*63*). Groups with low gene expression were removed from analysis. Seurat packages were also used for CCA (canonical correlation analysis)–based integration studies (*63*). Seurat-based software was used to generate DEGs, featureplots, dot plots, and violin plots. Differential expression for a specific cluster was determined by comparison against all other clusters.

Macrophage/DC DEG lists were queried against the Immgen gene expression database (www.immgen.org) using the interactive tool "My Gene Set" to identify functional cell types and against the Database for Annotation, Visualization and Integrated Discovery (DAVID) functional annotation tools (David.ncifrf.gov) and STRING-compiled databases (string-db.org) to generate functional enrichment lists from GO (biological process, molecular function, and cellular component) KEGG, and Reactome pathways.

PCR and qRT-PCR

RNA from whole tissue, sorted, or cultured cells was isolated using RNeasy kits (QIAGEN). RNA concentration was assessed using a

NanoDrop 2000c spectrophotometer (Thermo Fisher Scientific), and purity was assessed by labchip analyses (Agilent RNA 6000 Pico Kit). Roughly equal amounts of RNA were converted to complementary DNA using the Superscript IV Vilo Kit (Thermo Fisher Scientific), and qRT-PCR was performed using a StepOnePlus Real-Time PCR System (Applied Biosystems) with TaqMan primer/probe sets from Applied Biosystems. Reactions were performed as described (*22*), and relative expression levels were standardized using housekeeping genes glyceraldehyde phosphate dehydrogenase (GAPDH) and/or 18*S* ribosomal RNA (rRNA) as internal controls. Results were obtained by the comparative C_T method (*64*) and expressed as fold change with respect to the experimental control (typically 18*S* rRNA). A single reference from either WIHN$^+$ or WT group (depending on the comparison) was set at 1 and applied to all samples. Because multiple samples were included within the "reference" set, final values reflect those of the entire set.

Lentiviral transduction of primary cell cultures

Dissociated WD11 and WD12 dermal cells were seeded in Dulbecco's modified Eagle's medium high glucose, GlutaMAX, pyruvate (Thermo Fisher Scientific) containing 10% HyClone Serum (GE Healthcare), and 1% penicillin-streptomycin and adherent cells (myofibroblasts) were maintained for 6 to 10 days with changes in medium every 2 to 3 days. Myofibroblasts were transduced at a 5:1 virus-to-cell ratio with GFP-tagged control or mouse SFRP4 shRNA-containing lentiviral particles (SMARTvector, Dharmacon) for 48 hours, followed by puromycin selection (2 μg/ml; Sigma P9620) for 48 hours. Cells were finally cultured in medium containing doxycycline hyclate (1 μg/ml; Sigma D9891) and WNT3a (1 ng/ml; R&D Systems) for 48 hours, followed by assaying for GFP$^+$ cells by cytofluorography (populations were >70%$^+$) and *SFRP4* and *Axin2* transcription by qRT-PCR.

Protein and Western analyses

To assess the content of the FN EDA splice variant, adult human FN (ScienCell 8488) and newborn human FN (Sigma F2518) proteins underwent reduction and electrophoresis onto a 3 to 8% tris-acetate gradient gel (NuPAGE) and blotting onto Immobilon-FL polyvinylidene difluoride membrane (Millipore). The membrane was probed with rabbit anti-FN (Abcam) and mouse anti–EDA-FN (Ist-9) antibodies followed by IRDye 800CW– or IRDye 680–conjugated secondary antibodies (LI-COR Biosciences), and immunofluorescence was detected using the Odyssey Infrared Imaging System (LI-COR Biosciences). Pull-down assays were undertaken by coincubating 10 μg of adult or newborn FN with or without 5 μg of recombinant human SFRP4 (R&D Systems) in Dulbecco's PBS containing Mg^{2+}, Ca^{2+}, 0.1% CHAPS, 0.1% octylglucoside, BSA (1 mg/ml), and 2% glycerol 4°C overnight then with rabbit anti-SFRP4 antibody loaded onto protein A agarose beads for 4 hours. Eluted proteins were run on a single gradient gel subsequently halved. Upper and lower halves were subjected to blotting conditions appropriate for transfer of either high or low molecular weight proteins, respectively. Blots were stained and read as described above. Relative protein densities were determined by ImageJ.

Statistical analyses

P values (two-tailed Student's *t* test) for a single variable between different groups, a Pearson correlation coefficient (ρ) for two variables within a single population, were both determined using Excel (Microsoft). $P < 0.05$ was considered significant. Data were expressed as means ± SEM. One-way multivariate analysis of variance (MANOVA; $\alpha = 0.05$) and univariate ANOVA analyses were computed using an IBM SSPS Statistics software (IBM) for Windows 7 (Build 1.0.0.781, 64-bit edition). $P < 0.0005$ was considered significant. Univariate ANOVAs were computed using IBM SSPS Statistics software (IBM) for Windows 7 (Build 1.0.0.781, 64-bit edition). $P < 0.005$ was considered significant.

SUPPLEMENTARY MATERIALS

Supplementary material for this article is available at http://advances.sciencemag.org/cgi/content/full/6/12/eaay3704/DC1

Fig. S1. WIHN$^-$ wounds have higher numbers of cells with nuclear β-Cat.
Fig. S2. Whole wound dermis and myofibroblast comparisons in WIHN$^+$ and WIHN$^-$ wounds.
Fig. S3. Comparisons of macrophage/DC populations in WIHN$^+$ and WIHN$^-$ wounds.
Fig. S4. WD16 wound examined for macrophage marker expression.
Fig. S5. Lower macrophage numbers in the late wound dermis correlate with reduced wound collagen.
Fig. S6. SFRP4 is located within lower wound dermis ECM and macrophages.
Fig. S7. Hemin abrogates phagocytosis in cultured macrophages but does not alter wound healing, wound architecture, or wound macrophage numbers in vivo.
Fig. S8. EDA-FN, *Tlr4*, and integrin studies.
Fig. S9. Comparisons of WT, *EDA-FN*$^{-/-}$, and *EDA-FN*$^{+/-}$ wounds.
Fig. S10. SFRP4 is phagocytized and degraded by CD68$^+$ macrophages in newly wounded HS skin dermis.
Fig. S11. Examination of ECM components and macrophages/DCs in human normal and HS skin.
Fig. S12. A proposed model for macrophage phagocytosis contribution to fibrosis.
Table S1. Gene signatures of myofibroblast groups I to III.
Table S2. STRING analyses of WIHN$^+$ and WIHN$^-$ macrophage clusters.
Table S3. List of the top 200 genes shared by macrophage subsets from integrated macrophage/DC analysis.
Movie S1. Localization of external SFRP4 and SFRP4 vesicles within MerTK$^+$ macrophage.

View/request a protocol for this paper from *Bio-protocol*.

REFERENCES AND NOTES

1. M. F. Beers, E. E. Morrisey, The three R's of lung health and disease: Repair, remodeling, and regeneration. *J. Clin. Invest.* **121**, 2065–2073 (2011).
2. A. Pellicoro, P. Ramachandran, J. P. Iredale, J. A. Fallowfield, Liver fibrosis and repair: Immune regulation of wound healing in a solid organ. *Nat. Rev. Immunol.* **14**, 181–194 (2014).
3. M. Edeling, G. Ragi, S. Huang, H. Pavenstädt, K. Susztak, Developmental signalling pathways in renal fibrosis: The roles of Notch, Wnt and Hedgehog. *Nat. Rev. Nephrol.* **12**, 426–439 (2016).
4. P. Muñoz-Cánoves, A. L. Serrano, Macrophages decide between regeneration and fibrosis in muscle. *Trends Endocrinol. Metab.* **26**, 449–450 (2015).
5. S. A. Eming, P. Martin, M. Tomic-Canic, Wound repair and regeneration: Mechanisms, signaling, and translation. *Sci. Transl. Med.* **6**, 265sr6 (2014).
6. F. Klingberg, B. Hinz, E. S. White, The myofibroblast matrix: Implications for tissue repair and fibrosis. *J. Pathol.* **229**, 298–309 (2013).
7. M. V. Plikus, C. F. Guerrero-Juarez, M. Ito, Y. R. Li, P. H. Dedhia, Y. Zheng, M. Shao, D. L. Gay, R. Ramos, T.-C. Hsi, J. W. Oh, X. Wang, A. Ramirez, S. E. Konopelski, A. Elzein, A. Wang, R. J. Supapannachart, H.-L. Lee, C. H. Lim, A. Nace, A. Guo, E. Treffeisen, T. Andl, R. N. Ramirez, R. Murad, S. Offermanns, D. Metzger, P. Chambon, A. D. Widgerow, T.-L. Tuan, A. Mortazavi, R. K. Gupta, B. A. Hamilton, S. E. Millar, P. Seale, W. S. Pear, M. A. Lazar, G. Cotsarelis, Regeneration of fat cells from myofibroblasts during wound healing. *Science* **355**, 748–752 (2017).
8. R. R. Driskell, B. M. Lichtenberger, E. Hoste, K. Kretzschmar, B. D. Simons, M. Charalambous, S. R. Ferron, Y. Herault, G. Pavlovic, A. C. Ferguson-Smith, F. M. Watt, Distinct fibroblast lineages determine dermal architecture in skin development and repair. *Nature* **504**, 277–281 (2013).
9. Y. Rinkevich, G. G. Walmsley, M. S. Hu, Z. N. Maan, A. M. Newman, M. Drukker, M. Januszyk, G. W. Krampitz, G. C. Gurtner, H. P. Lorenz, I. L. Weissman, M. T. Longaker, Identification and isolation of a dermal lineage with intrinsic fibrogenic potential. *Science* **348**, aaa2151 (2015).
10. M. Sigal, C. Y. Logan, M. Kapalczynska, H.-J. Mollenkopf, H. Berger, B. Wiedenmann, R. Nusse, M. R. Amieva, T. F. Meyer, Stromal R-spondin orchestrates gastric epithelial stem cells and gland homeostasis. *Nature* **548**, 451–455 (2017).
11. M. Roulis, R. A. Flavell, Fibroblasts and myofibroblasts of the intestinal lamina propria in physiology and disease. *Differentiation* **92**, 116–131 (2016).

12. B. Hinz, The extracellular matrix and transforming growth factor-β1: Tale of a strained relationship. *Matrix Biol.* **47**, 54–65 (2015).
13. J. S. Munger, D. Sheppard, Cross talk among TGF-β signaling pathways, integrins, and the extracellular matrix. *Cold Spring Harb. Perspect. Biol.* **3**, a005017 (2011).
14. Y. Guo, L. Xiao, L. Sun, F. Liu, Wnt/β-catenin signaling: A promising new target for fibrosis diseases. *Physiol. Res.* **61**, 337–346 (2012).
15. A. Akhmetshina, K. Palumbo, C. Dees, C. Bergmann, P. Venalis, P. Zerr, A. Horn, T. Kireva, C. Beyer, J. Zwerina, H. Schneider, A. Sadowski, M.-O. Riener, O. A. MacDougald, O. Distler, G. Schett, J. H. W. Distler, Activation of canonical Wnt signalling is required for TGF-β-mediated fibrosis. *Nat. Commun.* **3**, 735 (2012).
16. D. Bastakoty, S. Saraswati, J. Cates, E. Lee, L. B. Nanney, P. P. Young, Inhibition of Wnt/β-catenin pathway promotes regenerative repair of cutaneous and cartilage injury. *FASEB J.* **29**, 4881–4892 (2015).
17. B. Piersma, R. A. Bank, M. Boersema, Signaling in fibrosis: TGF-β, WNT, and YAP/TAZ converge. *Front. Med.* **2**, 59 (2015).
18. E. J. Hamburg, R. P. Atit, Sustained β-catenin activity in dermal fibroblasts is sufficient for skin fibrosis. *J. Invest. Dermatol.* **132**, 2469–2472 (2012).
19. E. Hamburg-Shields, G. J. DiNuoscio, N. K. Mullin, R. Lafyatis, R. P. Atit, Sustained β-catenin activity in dermal fibroblasts promotes fibrosis by up-regulating expression of extracellular matrix protein-coding genes. *J. Pathol.* **235**, 686–697 (2015).
20. M. Mastrogiannaki, B. M. Lichtenberger, A. Reimer, C. A. Collins, R. R. Driskell, F. M. Watt, β-catenin stabilization in skin fibroblasts causes fibrotic lesions by preventing adipocyte differentiation of the reticular dermis. *J. Invest. Dermatol.* **136**, 1130–1142 (2016).
21. D. Gay, O. Kwon, Z. Zhang, M. Spata, M. V. Plikus, P. D. Holler, M. Ito, Z. Yang, E. Treffeisen, C. D. Kim, A. Nace, X. Zhang, S. Baratono, F. Wang, D. M. Ornitz, S. E. Millar, G. Cotsarelis, Fgf9 from dermal γδ T cells induces hair follicle neogenesis after wounding. *Nat. Med.* **19**, 916–923 (2013).
22. A. B. Aurora, E. N. Olson, Immune modulation of stem cells and regeneration. *Cell Stem Cell* **15**, 14–25 (2014).
23. T. A. Wynn, K. M. Vannella, Macrophages in tissue repair, regeneration, and fibrosis. *Immunity* **44**, 450–462 (2016).
24. T. Lucas, A. Waisman, R. Ranjan, J. Roes, T. Krieg, W. Müller, A. Roers, S. A. Eming, Differential roles of macrophages in diverse phases of skin repair. *J. Immunol.* **184**, 3964–3977 (2010).
25. A. J. Lechner, I. H. Driver, J. Lee, C. M. Conroy, A. Nagle, R. M. Locksley, J. R. Rock, Recruited monocytes and Type 2 immunity promote lung regeneration following pneumonectomy. *Cell Stem Cell* **21**, 120–134.e7 (2017).
26. J. A. Knipper, S. Willenborg, J. Brinckmann, W. Bloch, T. Maaß, R. Wagener, T. Krieg, T. Sutherland, A. Munitz, M. E. Rothenberg, A. Niehoff, R. Richardson, M. Hammerschmidt, J. E. Allen, S. A. Eming, Interleukin-4 receptor α signaling in myeloid cells controls collagen fibril assembly in skin repair. *Immunity* **43**, 803–816 (2015).
27. P. J. Murray, Macrophage polarization. *Annu. Rev. Physiol.* **79**, 541–566 (2017).
28. Y. Kumamoto, J. P. G. Camporez, M. J. Jurczak, M. Shanabrough, T. Horvath, G. I. Shulman, A. Iwasaki, CD301b$^+$ mononuclear phagocytes maintain positive energy balance through secretion of resistin-like molecule alpha. *Immunity* **45**, 583–596 (2016).
29. J. J. Lim, S. Grinstein, Z. Roth, Diversity and versatility of phagocytosis: Roles in innate immunity, tissue remodeling, and homeostasis. *Front. Cell. Infect. Microbiol.* **7**, 191 (2017).
30. M. Morikawa, S. Tsujibe, J. Kiyoshima-Shibata, Y. Watanabe, N. Kato-Nagaoka, K. Shida, S. Matsumoto, Microbiota of the small intestine is selectively engulfed by phagocytes of the lamina propria and Peyer's patches. *PLOS ONE* **11**, e0163607 (2016).
31. D. H. Madsen, D. Leonard, A. Masedunskas, A. Moyer, H. J. Jürgensen, D. E. Peters, P. Amornphimoltham, A. Selvaraj, S. S. Yamada, D. A. Brenner, S. Burgdorf, L. H. Engelholm, N. Behrendt, K. Holmbeck, R. Weigert, T. H. Bugge, M2-like macrophages are responsible for collagen degradation through a mannose receptor–mediated pathway. *J. Cell Biol.* **202**, 951–966 (2013).
32. C. Breedis, Regeneration of hair follicles and sebaceous glands from the epithelium of scars in the rabbit. *Cancer Res.* **14**, 575–579 (1954).
33. M. Ito, Z. Yang, T. Andl, C. Cui, N. Kim, S. E. Millar, G. Cotsarelis, Wnt-dependent de novo hair follicle regeneration in adult mouse skin after wounding. *Nature* **447**, 316–320 (2007).
34. X. Wang, H. Chen, R. Tian, Y. Zhang, M. S. Drutskaya, C. Wang, J. Ge, Z. Fan, D. Kong, X. Wang, T. Cai, Y. Zhou, J. Wang, J. Wang, S. Wang, Z. Qin, H. Jia, Y. Wu, J. Liu, S. A. Nedospasov, E. E. Tredget, M. Lin, J. Liu, Y. Jiang, Y. Wu, Macrophages induce AKT/β-catenin-dependent Lgr5$^+$ stem cell activation and hair follicle regeneration through TNF. *Nat. Commun.* **8**, 14091 (2017).
35. A. Kasuya, T. Ito, Y. Tokura, M2 macrophages promote wound-induced hair neogenesis. *J. Dermatol. Sci.* **91**, 250–255 (2018).
36. B. A. Shook, R. R. Wasko, G. C. Rivera-Gonzalez, E. Salazar-Gatzimas, F. López-Giráldez, B. C. Dash, A. R. Muñoz-Rojas, K. D. Aultman, R. K. Zwick, V. Lei, J. L. Arbiser, K. Miller-Jensen, D. A. Clark, H. C. Hsia, V. Horsley, Myofibroblast proliferation and heterogeneity are supported by macrophages during skin repair. *Science* **362**, eaar2971 (2018).
37. C. F. Guerrero-Juarez, P. H. Dedhia, S. Jin, R. Ruiz-Vega, D. Ma, Y. Liu, K. Yamaga, O. Shestova, D. L. Gay, Z. Yang, K. Kessenbrock, Q. Nie, W. S. Pear, G. Cotsarelis, M. V. Plikus, Single-cell analysis reveals fibroblast heterogeneity and myeloid-derived adipocyte progenitors in murine skin wounds. *Nat. Commun.* **10**, 650 (2019).
38. T. Iwayama, C. Steele, L. Yao, M. G. Dozmorov, D. Karamichos, J. D. Wren, L. E. Olson, PDGFRα signaling drives adipose tissue fibrosis by targeting progenitor cell plasticity. *Genes Dev.* **29**, 1106–1119 (2015).
39. J. M. Poczobutt, S. De, V. K. Yadav, T. T. Nguyen, H. Li, T. R. Sippel, M. C. M. Weiser-Evans, R. A. Nemenoff, Expression profiling of macrophages reveals multiple populations with distinct biological roles in an immunocompetent orthotopic model of lung cancer. *J. Immunol.* **196**, 2847–2859 (2016).
40. Y. Ishida, J.-L. Gao, P. M. Murphy, Chemokine receptor CX3CR1 mediates skin wound healing by promoting macrophage and fibroblast accumulation and function. *J. Immunol.* **180**, 569–579 (2008).
41. S. H. Burnett, E. J. Kershen, J. Zhang, L. Zeng, S. C. Straley, A. M. Kaplan, D. A. Cohen, Conditional macrophage ablation in transgenic mice expressing a Fas-based suicide gene. *J. Leukoc. Biol.* **75**, 612–623 (2004).
42. A. Sebastian, N. R. Hum, C. Morfin, D. K. Murugesh, G. G. Loots, Global gene expression analysis identifies Mef2c as a potential player in Wnt16-mediated transcriptional regulation. *Gene* **675**, 312–321 (2018).
43. R. Martins, J. Maier, A.-D. Gorki, K. V. M. Huber, O. Sharif, P. Starkl, S. Saluzzo, F. Quattrone, R. Gawish, K. Lakovits, M. C. Aichinger, B. Radic-Sarikas, C.-H. Lardeau, A. Hladik, A. Korosec, M. Brown, K. Vaahtomeri, M. Duggan, D. Kerjaschki, H. Esterbauer, J. Colinge, S. C. Eisenbarth, T. Decker, K. L. Bennett, S. Kubicek, M. Sixt, G. Superti-Furga, S. Knapp, Heme drives hemolysis-induced susceptibility to infection via disruption of phagocyte functions. *Nat. Immunol.* **17**, 1361–1372 (2016).
44. J.-L. Lee, C.-T. Lin, L.-L. Chueh, C.-J. Chang, Autocrine/paracrine secreted frizzled-related protein 2 induces cellular resistance to apoptosis: A possible mechanism of mammary tumorigenesis. *J. Biol. Chem.* **279**, 14602–14609 (2004).
45. C. Ffrench-Constant, L. Van de Water, H. F. Dvorak, R. O. Hynes, Reappearance of an embryonic pattern of fibronectin splicing during wound healing in the adult rat. *J. Cell Biol.* **109**, 903–914 (1989).
46. S. Bhattacharyya, Z. Tamaki, W. Wang, M. Hinchcliff, P. Hoover, S. Getsios, E. S. White, J. Varga, Fibronectin^{EDA} promotes chronic cutaneous fibrosis through toll-like receptor signaling. *Sci. Transl. Med.* **6**, 232ra50 (2014).
47. R. M. Kelsh-Lasher, A. Ambesi, C. Bertram, P. J. McKeown-Longo, Integrin α4β1 and TLR4 cooperate to induce fibrotic gene expression in response to fibronectin's EDA domain. *J. Invest. Dermatol.* **137**, 2505–2512 (2017).
48. Z. Julier, M. M. Martino, A. de Titta, L. Jeanbart, J. A. Hubbell, The TLR4 agonist fibronectin extra domain A is cryptic, exposed by elastase-2; use in a fibrin matrix cancer vaccine. *Sci. Rep.* **5**, 8569 (2015).
49. S. D. Blystone, I. L. Graham, F. P. Lindberg, E. J. Brown, Integrin alpha v beta 3 differentially regulates adhesive and phagocytic functions of the fibronectin receptor alpha 5 beta 1. *J. Cell Biol.* **127**, 1129–1137 (1994).
50. A. F. Muro, A. K. Chauhan, S. Gajovic, A. Iaconcig, F. Porro, G. Stanta, F. E. Baralle, Regulated splicing of the fibronectin EDA exon is essential for proper skin wound healing and normal lifespan. *J. Cell Biol.* **162**, 149–160 (2003).
51. E. Prens, I. Deckers, Pathophysiology of hidradenitis suppurativa: An update. *J. Am. Acad. Dermatol.* **73**, S8–S11 (2015).
52. A. Shah, R. Alhusayen, S. Amini-Nik, The critical role of macrophages in the pathogenesis of hidradenitis suppurativa. *Inflamm. Res.* **66**, 931–945 (2017).
53. M. A. Gray, C. H. Choy, R. M. Dayam, E. Ospina-Escobar, A. Somerville, X. Xiao, S. M. Ferguson, R. J. Botelho, Phagocytosis enhances lysosomal and bactericidal properties by activating the transcription factor TFEB. *Curr. Biol.* **26**, 1955–1964 (2016).
54. T. Xie, Y. Wang, N. Deng, G. Huang, F. Taghavifar, Y. Geng, N. Liu, V. Kulur, C. Yao, P. Chen, Z. Liu, B. Stripp, J. Tang, J. Liang, P. W. Noble, D. Jiang, Single-cell deconvolution of fibroblast heterogeneity in mouse pulmonary fibrosis. *Cell Rep.* **22**, 3625–3640 (2018).
55. C.-C. Chen, L. Wang, M. V. Plikus, T. X. Jiang, P. J. Murray, R. Ramos, C. F. Guerrero-Juarez, M. W. Hughes, O. K. Lee, S. Shi, R. B. Widelitz, A. D. Lander, C. M. Chuong, Organ-level quorum sensing directs regeneration in hair stem cell populations. *Cell* **161**, 277–290 (2015).
56. E. Rognoni, C. Gomez, A. O. Pisco, E. L. Rawlins, B. D. Simons, F. M. Watt, R. R. Driskell, Inhibition of β-catenin signalling in dermal fibroblasts enhances hair follicle regeneration during wound healing. *Development* **143**, 2522–2535 (2016).
57. D. Chen, A. Jarrell, C. Guo, R. Lang, R. Atit, Dermal β-catenin activity in response to epidermal Wnt ligands is required for fibroblast proliferation and hair follicle initiation. *Development* **139**, 1522–1533 (2012).
58. C. H. Lim, Q. Sun, K. Ratti, S.-H. Lee, Y. Zheng, M. Takeo, W. Lee, P. Rabbani, M. V. Plikus, J. E. Cain, D. H. Wang, D. N. Watkins, S. Millar, M. M. Taketo, P. Myung, G. Cotsarelis, M. Ito, Hedgehog stimulates hair follicle neogenesis by creating inductive dermis during murine skin wound healing. *Nat. Commun.* **9**, 4903–4913 (2018).

59. P. Bovolenta, P. Esteve, J. M. Ruiz, E. Cisneros, J. Lopez-Rios, Beyond Wnt inhibition: New functions of secreted Frizzled-related proteins in development and disease. *J. Cell Sci.* **121**, 737–746 (2008).
60. G. H. Dolmans, P. M. Werker, H. C. Hennies, D. Furniss, E. A. Festen, L. Franke, K. Becker, P. van der Vlies, B. H. Wolffenbuttel, S. Tinschert, M. R. Toliat, M. Nothnagel, A. Franke, N. Klopp, H.-E. Wichmann, P. Nürnberg, H. Giele, R. A. Ophoff, C. Wijmenga; Dutch Dupuytren Study Group; German Dupuytren Study Group; LifeLines Cohort Study; BSSH–GODD Consortium, Wnt signaling and Dupuytren's disease. *N. Engl. J. Med.* **365**, 307–317 (2011).
61. P. D. Arora, M. F. Manolson, G. P. Downey, J. Sodek, C. A. G. McCulloch, A novel model system for characterization of phagosomal maturation, acidification, and intracellular collagen degradation in fibroblasts. *J. Biol. Chem.* **275**, 35432–35441 (2000).
62. D. L. Gay, C.-C. Yang, M. V. Plikus, M. Ito, C. Rivera, E. Treffeisen, L. Doherty, M. Spata, S. E. Millar, G. Cotsarelis, CD133 expression correlates with membrane beta-catenin and E-cadherin loss from human hair follicle placodes during morphogenesis. *J. Invest. Dermatol.* **135**, 45–55 (2015).
63. A. Butler, P. Hoffman, P. Smibert, E. Papalexi, R. Satija, Integrating single-cell transcriptomic data across different conditions, technologies, and species. *Nat. Biotechnol.* **36**, 411–420 (2018).
64. K. J. Livak, T. D. Schmittgen, Analysis of relative gene expression data using real-time quantitative PCR and the $2^{-\Delta\Delta C}_{T}$ Method. *Methods* **25**, 402–408 (2001).

Acknowledgments: We wish to thank Q. Sun (New York University Langone Medical Center, New York, NY), S. Moreno, and C. Torres for thoughtful suggestions; C. Joubert and V. Durand for assistance with animal protocols (CEA, Fontenay-aux-Roses cedex, France) and A. Muro (ICGEB, Trieste, Italy), D. O'Gorman (University of Western Ontario, London, Canada), and M. M. Marks (University of Pennsylvania, Philadelphia, USA) for providing valuable information about *EDA-FN*$^{+/-}$ mice and Dupuytren's syndrome and help with experimental design, respectively; S. Aractingi (Hôpital Cochin and Université Paris Descartes, Paris, France) for valuable insight into HS; J. C. Simon, M. Ziemer, S. Grunewald, and J. Thees (Department of Dermatology, University Leipzig Medical Center, Leipzig, Germany) for help in accessing HS tissues; and the NYUMC Genome Technology Center (in particular, A. Heguy, Y. Zhang, and C. Marier) for expert assistance with library preparation, Illumina sequencing and Cell Ranger alignment. **Funding:** D.G. has salary support from INSERM and CEA funding. This work was supported by grants from Inserm, CEA, University Paris-Diderot, and University Paris-Sud. M.V.P. is supported by the NIH NIAMS grants R01-AR067273 and R01-AR069653 and Pew Charitable Trust grant. C.F.G.-J. is supported by the UC Irvine Chancellor's ADVANCE Postdoctoral Fellowship Program, an NSF-Simons Postdoctoral Fellowship, NSF Grant DMS1763272, and Simons Foundation Grant 594598. R.A.F. is supported by a DFG grant FE 1850/1-1. S.F. is supported by the German Research Council DFG SFB-TR67 project B3 and DFG grant FR2671/4-1. M.I. and C.H.L. partial support is through NIH NIAMS R01-AR059768 and R01-AR066022. The NYU Langone Genome Technology Center is partially supported by grant NIH NCI P30CA016087. **Author contributions:** D.G. conceived of and designed all experiments with substantial contributions from P.-H.R. D.G. and G.G. conducted experiments, data analyses, and interpretation with help from S.M. D.G. wrote the manuscript with editorial assistance from P.-H.R. and M.V.P. C.F.G-J undertook ANOVA and MANOVA statistical analyses. R.A.F. provided expertise and human samples for HS studies. N.G., V.B., I.R., P.M., L.I., and E.T. provided technical support for cell sorting, genotyping, animal care, confocal microscopy. D.G and C.H.L. conducted experiments for single-cell RNA-seq. D.G. and F.F. analyzed RNA-seq results. E.T. provided graphical illustrations. F.F., S.F., A.B., C.C., M.I., and M.V.P. provided intellectual support and scientific expertise. **Competing interests:** The authors declare that they have no competing interests. **Data and materials availability:** The GEO accession number for single-cell RNA-seq analyses is GSE141814. All other data needed to evaluate the conclusions in the paper are present in the paper and/or the Supplementary Materials. Additional data related to this paper may be requested from the authors.

Submitted 12 June 2019
Accepted 20 December 2019
Published 20 March 2020
10.1126/sciadv.aay3704

Citation: D. Gay, G. Ghinatti, C. F. Guerrero-Juarez, R. A. Ferrer, F. Ferri, C. H. Lim, S. Murakami, N. Gault, V. Barroca, I. Rombeau, P. Mauffrey, L. Irbah, E. Treffeisen, S. Franz, A. Boissonnas, C. Combadière, M. Ito, M. V. Plikus, P.-H. Romeo, Phagocytosis of Wnt inhibitor SFRP4 by late wound macrophages drives chronic Wnt activity for fibrotic skin healing. *Sci. Adv.* **6**, eaay3704 (2020).

Science Advances

Phagocytosis of Wnt inhibitor SFRP4 by late wound macrophages drives chronic Wnt activity for fibrotic skin healing

Denise Gay, Giulia Ghinatti, Christian F. Guerrero-Juarez, Rubén A. Ferrer, Federica Ferri, Chae Ho Lim, Shohei Murakami, Nathalie Gault, Vilma Barroca, Isabelle Rombeau, Philippe Mauffrey, Lamya Irbah, Elsa Treffeisen, Sandra Franz, Alexandre Boissonnas, Christophe Combadière, Mayumi Ito, Maksim V. Plikus and Paul-Henri Romeo

Sci Adv **6** (12), eaay3704.
DOI: 10.1126/sciadv.aay3704